Space–time dynamics of optimal wavepackets for streaks in a channel entrance flow

F. Alizard, A. Cadiou, L. Le Penven, B. Di Pierro, M. Buffat

Space-time dynamics of optimal wavepackets for streaks in a channel entrance flow

F. Alizard, A. Cadiou, L. Le Penven, B. Di Pierro and M. Buffat

May 24, 2017

Abstract

Laminar/turbulent transition of a channel entrance flow for uniform inlet condition is revisited using global linear optimization analyses and direct numerical simulations. This work focuses on the region near the inlet, for a subcritical Reynolds number flow. The laminar flow developing from the entrance is linearly stable, but when perturbed by local optimal modes from the inlet section can give rise to steady nonlinear streaks, developing in the boundary layers on the walls. In this study, only the lower wall is perturbed. The boundary layers are asymptotically stable, however, a secondary linear instability analysis shows that for sufficiently high amplitude of the streaks, global optimal modes, both varicose and sinuous, taking the form of wavepackets, are amplified. It is shown that for short optimization times, varicose wavepacket grows through a combination of the Orr and lift-up effects, whereas for larger target times, both sinuous and varicose wavepackets (if exist) exhibit an instability mechanism driven by the presence of inflection points in the streaky flow. In addition, while the initial conditions for the optimal varicose modes obtained for short optimization times are localized near the inlet, where the base flow is strongly three-dimensional, the sinuous and varicose optimal modes are displaced further downstream, in the nearly parallel streaky flow, when the target time is increased. Finally, the effects of nonlinearities are highlighted by investigating the space-time evolution of the optimal wavepackets when superimposed to the streaky flow with a sufficiently high amplitude to trigger breakdown to turbulence. It is noticed that the resulting turbulent flow have the same wall-shear stress, whether the wavepackets have been obtained for short or for long time optimization.

1 Introduction

Transition from laminar to turbulent of wall bounded flows has traditionally been studied by considering the case of the Blasius boundary layer and the Poiseuille channel flow while less attention has been paid to flow developing in the entrance region. The latter problem remains of fundamental importance for giving a better understanding of transition in channel or pipe where differences between theoretical, numerical and experimental approaches are frequently attributed to flow development effects (see [1] for the pipe flow case for instance). In the entrance region of the plane channel, at sufficiently high Reynolds number, the flow is characterized by the development of boundary layers along the two flat plates that merge far downstream. Both boundary layers are subjected to a favorable pressure gradient due to the confinement effect.

It has for consequence to stabilize the flow with respect to the so-called Tollmien-Schlichting mode. Up to now, linear theories fail to ascribe subcritical transition observed in the plane channel flow to stability properties of the streamwise velocity profiles in the channel entry flow, as shown by Biau [2]. However, these theoretical studies focus on the region downstream the entry zone where the evolution of the flow has a universal character (see Asai and Floryan [3]) and therefore are not directly connected to the flow behaviour near the inlet. The major difficulty is that near the leading edges the flow is strongly dependent of the inlet geometry as well as of the prescribed inflow velocity, as shown for instance by Sadri and Floryan [4]. For the case where the inflow condition is uniform at the inlet, Buffat et al. [5] have recently shown by direct numerical simulations (DNS) that, while boundary layers near the entrance are linearly stable for exponentially growing modes, they may experience laminar/turbulent transition well before their achievement to a fully developed flow (i.e. the Poiseuille flow solution). They show that transition occurs by secondary instability of streaks (elongated regions of excess or defect of streamwise velocity) leading to a rapid breakdown to turbulence. In their study, streaks have been generated by superimposing the optimal mode of the linear stability analysis of the inlet velocity profile. The optimal modes consist of a pair of streamwise vortices, located inside the laminar boundary layer at the entrance of the channel. The streaks are amplified due to the so-called lift-up mechanism [6] that yields to a significant nonlinear growth, resulting in strongly distorted streaks compared to their linear counterparts. In that way, the path leading to a turbulent flow highlighted by Buffat et al. [7] exhibits a strong resemblance to the bypass scenario for a flat plate boundary layer flow (see for instance Brandt and Henningson [8], Zaki and Durbin [9] and Durbin and Wu [10]). Buffat et al. [5] also show that the fully developed turbulent regime downstream is similar to a turbulent channel flow. Despite these similarities, the bypass transition scenario observed by the latter authors differs in some points from previous DNS of streak breakdown. While it is commonly accepted that streak breakdown is often caused by sinuous instability (i.e. an anti-symmetric pattern with respect to the low-speed streak), Buffat et al. [5] show that streaks experience a transient varicose instability (i.e. characterized by a symmetric pattern) near the inlet before to be dominated by a sinuous motion.

Andersson et al. [11] carried out the first linear stability analysis on a frozen streamwise invariant streaky boundary layer flow with various amplitudes. They reported the onset of high-frequencies modal secondary instabilities for critical streak amplitudes of 26% and 37% for the sinuous and varicose modes, respectively. The varicose instability is usually related to wall normal inflectional velocity profiles whereas the sinuous one to the presence of inflection points along the spanwise direction. This scenario is generally observed. However, Brandt [12] reported that for a specific low-speed streak shape, sinuous instability may be amplified due to the wall-normal shear. Nevertheless, discrepancies still remain between critical streak amplitudes predicted by modal linear stability theory and experiments, as reported by Matsubara and Alfredsson [13], Mandal et al. [14] where streak breakdown is observed for significantly lower streak amplitudes. These last few years, many explanations have been addressed trying to fill the gap between theoretical and experimental observed thresholds. Vaughan and Zaki [15] and Hack and Zaki [16] suggest that discrepancies can be overtaken by considering more realistic streaks (i.e. having a finite size in the streamwise direction and being unsteady). Brandt and de Lange [17] show that streak collisions may lead to breakdown to turbulence for critical streak amplitudes lower than the ones predicted by a modal linear stability theory. Finally, it is also clear that bifurcations of streaks may not be necessary attributed to a secondary

modal instability. Since the preliminary work of Schoppa and Hussain [18] that deals with streaks populating the near-wall region of a turbulent channel flow, a viable scenario relying on a breakdown mechanism triggered by the transient growth of secondary perturbations have emerged. In particular, optimal modes having the highest potential in transient energy growth are computed for idealized streaks that are invariants with respect to the streamwise direction by Hoepffner et al. [19] and Cossu et al. [20], for flat plate boundary layer and channel flows. The previous authors show that streaks may sustain large transient energy growth for both sinuous and varicose symmetries at amplitudes significantly below the critical value beyond which streaks are unstable with respect to an exponentially growing mode. In particular, Hoepffner et al. [19] highlight the importance of Orr [21] and lift-up [6] mechanisms in extracting energy from the base flow. The subcritical behaviour of streaks is further investigated by Cossu et al. [22] for the case of a channel flow. The authors carried out nonlinear simulations in the $A_U - A_W$ plane, where A_U and A_W are associated with the nonlinear saturated streaks amplitude and the amplitude of the secondary perturbation, respectively. Cossu et al. [22] found that transition due to a modal instability is given for large streak amplitude and small amplitudes for the secondary perturbations. Streaks breakdown caused by a transient growth of secondary perturbations is obtained for significantly smaller streaks amplitudes. In the former study, it is clearly enlightened that a full understanding of bypass transition scenario is not only provided by the aim of computing streaks amplitude giving rise to a modal instability but should also take into account the amplitude of secondary perturbations and nonlinear effects.

Recently, Cherubini et al. [23] carried out linear global optimizations (i.e. relying on a three-dimensional basic state and aiming to compute localized perturbations in space inducing the largest transient energy growth for a given time) for boundary-layer flow in the presence of a smooth three-dimensional roughness element. In contrast to a parallel flat plate boundary layer flow, the authors show that for short optimization times, the highest potential in kinetic energy growth is obtained for a varicose symmetry. The three-dimensional optimal mode is seen to take the form of a localized wavepacket in the wake of the bump. In particular, by superimposing the optimal mode into the basic flow, the streaky motion behind the bump exhibits a subcritical bifurcation when the amplitude of the secondary perturbation is sufficiently large. It yields to the formation of hairpin packets that lead to laminar/turbulent transition.

The preceding discussion summarizes two mechanisms for which a streaky boundary layer flow undergoes a secondary instability: a modal instability, mainly associated with sinuous symmetry and a nonmodal mechanism where both the varicose and sinuous scenario may be viable. It may be suggested that streaks developing at the entrance of a channel flow can also support secondary instabilities for either a modal or nonmodal mechanism leading to turbulence. The present work thus aims to investigate the relevancy of the last mentioned scenario elaborated on a flat plate boundary layer for the case of the entrance channel flow and especially in a region far upstream the merging of the boundary layers. It is devoted to the study of the secondary instability mechanisms associated with steady streamwise varying streaks of various amplitudes, located near the entrance of a channel flow. Based on the recent analysis carried out by Cherubini et al. [23], instability properties is analyzed in the light of a global optimization framework allowing to consider both nonmodal and modal mechanisms (Orr and lift-up effects, and instability governed by inflection points, respectively) without any assumptions on the basic state. The present study address fundamental questions such as the following: do streaks developing near the inlet bifurcate by means of modal or nonmodal mechanisms ?

What are the physical mechanisms responsible for the growth of secondary instability for either the sinuous or varicose symmetry ? And what are the effects of nonlinearities associated with secondary instabilities and their consequences for driving the flow into a turbulent regime ?

The paper is organized as follows. In section 2, we formulate numerical methods and the optimization theory that are employed to investigate stability properties of the streaks near the entrance region. In section 3, after having presented the base flows associated with three different streaks amplitudes, we show the optimal modes and the underlying physical mechanisms responsible for the growth. In the light of these results, the influence of nonlinearities will be discussed by using Direct Numerical Simulations in section 4. The different paths leading to a fully turbulent channel flow associated with instabilities near the inlet region will be presented in section 5. Finally, section 6 is devoted in drawing conclusions and perspectives.

2 Theoretical background

2.1 Problem formulation

This paper is concerned with the stability properties of streaks embedded in a spatially developping plane channel flow. In the following, the variables are made dimensionless with the channel half-width h and the flow rate velocity U_0 across the channel inlet section, the Reynolds number is defined by $Re = U_0 h/\nu$ where ν is the kinematic viscosity. Using the cartesian coordinate system (x, y, z), the channel walls are the two semi-infinite planes $y = \pm 1$, $0 \leq x$ and the inlet section is at $x = 0$. We are especially interested in the entrance region, located downstream the inlet section, but still distant from the the fully-developped stage corresponding to Poiseuille solution ($x \sim Re$). The flow satisfies the incompressible Navier-Stokes equations:

$$\begin{aligned} &\frac{\partial \mathbf{u}}{\partial t} + (\mathbf{u} \cdot \nabla)\,\mathbf{u} = -\nabla p + \frac{1}{Re}\nabla^2 \mathbf{u}, \\ &\nabla \cdot \mathbf{u} = 0, \end{aligned} \tag{1}$$

and (u, v, w) will denote the cartesian components of the velocity $\mathbf{u}$. The base flow under study is specified by the velocity field $\mathbf{U}$, which is a steady solution of (1). This field splits into two parts : $\mathbf{U} = \mathbf{U}_{2D} + \mathbf{u}_S$. The first part $\mathbf{U}_{2D}$ is the two-dimensional steady solution of (1) obtained when imposing uniform velocity $\mathbf{U} = (1, 0, 0)$ in the freestream. At the value of Re considered hereafter, this flow consists of two Blasius-like boundary layers slowly evolving downstream towards the Poiseuille solution. It will be referred to as the primary base flow. The second part $\mathbf{u}_S$ is a disturbance that takes the form of a three-dimensional streamwise/streak pattern. The disturbance, referred to as the primary disturbance, is such that $\mathbf{U}$ satisfies (1) without linearization assumption at this stage. Our interest is in the space-time evolution of secondary perturbations $\mathbf{u}'$ superimposed to $\mathbf{U}$. Depending on whether we are interested in purely linear effects or in the non-linear regime, this evolution will be determined using the linearized version of (1) or its primitive form. The governing equations associated with the linear dynamics of $\mathbf{u}'$ are found by substituting $\mathbf{u} = \mathbf{U} + \varepsilon \mathbf{u}'$ and $p = P + \varepsilon p'$ (p' is the pressure perturbation) into

Flow cases	L_x	L_y	L_z	N_x	N_y	N_z
$\mathbf{U}_{2D}$	100	2		1920	193	
$\mathbf{U}$	100	2	λ_z	1920	193	24
$\mathbf{u}'$ (linear)	100	2	λ_z	1920	193	24
$\mathbf{U}+\mathbf{u}'$ (nonlinear)	100	2	$4\lambda_z$	1920	193	96

Table 1: Flow cases. The side lengths of the rectangular computational box are L_x, L_y and L_z for the streamwise, wall-normal and spanwise directions, respectively. N_x, N_y and N_z are the corresponding numbers of modes. $\lambda_z \simeq 1.14$ is the fundamental wave length of the primary disturbance (i.e. the vortex/streak pattern).

equations (1) and keeping only the first order in ε. It yields the following system:

$$\begin{aligned} \frac{\partial \mathbf{u}'}{\partial t} &= -\left(\mathbf{U}\cdot\nabla\right)\mathbf{u}' - \left(\mathbf{u}'\cdot\nabla\right)\mathbf{U} - \nabla p' + \frac{1}{Re}\nabla^2\mathbf{u}', \\ \nabla\cdot\mathbf{u}' &= 0, \end{aligned} \tag{2}$$

which is complemented by appropriate boundary and initial conditions.

2.2 Numerical methods

The numerical method is based on a spectral Galerkin approximation of the velocity fields using Fourier expansions in both the streamwise and spanwise directions and Chebyshev polynomials in the wall-normal direction. Using a divergence-free basis set of vectors, continuity is satisfied implicitely [24] and the pressure disappears from the discretized equation. To overcome the inherent difficulties when using Fourier modes along x, which is a direction of evolution for the flow, a fringe region technique is employed [25]. By adding a forcing term into the Navier-Stokes equations, the outgoing flow is smoothly driven to the prescribed inlet condition. In order to build the target velocity field which is used in the fringe region, a preliminary calculation of the primary base flow is carried out using a second-order finite difference code (see Nordstrom et al. [26]). The numerical method employed to compute this preliminary solution is detailed in Alizard et al. [27].

The discrete system attached to (1) is solved at each time step using a low storage semi-implicit third-order Runge-Kutta scheme. Viscous terms are treated implicitly while an explicit scheme is used for the convective term, as described by Spalart et al. [28]. Numerical methods are further detailed in Buffat et al. [7]. To solve the linearized problem (2), the coupling term with the base flow is also treated explicitely.

The different types of flow simulation investigated hereafter are listed in table 1, as with the chosen parameters of discretization. For all flow cases, the Reynolds number is fixed to $Re = 2500$ and the computation domain is comprised between $x = x_0$ and $x = x_0 + L_x$, with $x_0 = 16$ and $L_x = 100$. In the following, we will make use of the notation $x_i = x - x_0$ for the shifted streamwise coordinate. For all computations, the fringe region is located between $x_i = 0.9\,L_x$ and $x_i = L_x$.

2.3 Linear global optimization

In this section, we describe the method used to identify optimal perturbations i.e. perturbations undergoing the largest linear growth in energy for a given time horizon. Let us first write the solution of the linearized Navier-Stokes equations around the steady state (2) as :

$$\mathbf{u}'(t) = \mathcal{A}(t)\,\mathbf{u}'_0, \tag{3}$$

Under this form, in which the space variable is left out, the $\mathcal{A}(t)$ appears as a forward time-shift operator for the initial perturbation, $\mathbf{u}'(t=0) = \mathbf{u}'_0 \neq 0$. It is known that streaky boundary layer flows are absolutely stable and that they can exhibit large energy growth due to convective instabilities [29]. In fact, the dynamics of interest is quantified through the singular value decomposition of $\mathcal{A}(t)$. We introduce the kinetic energy norm associated with the L_2 inner product, noted herein as $<,>$ and focus on the space-time evolution of $\mathbf{u}'_0$, a perturbation given at $t = 0$ and having finite kinetic energy. The rate of change of perturbation energy is measured by:

$$\frac{E(t)}{E_0} = \frac{<\mathbf{u}'(t), \mathbf{u}'(t)>}{<\mathbf{u}'_0, \mathbf{u}'_0>}, \tag{4}$$

where $E_0 = E(t=0)$. Using (3), we define thus the optimal energy growth over all possible $\mathbf{u}'_0$ as:

$$\frac{E(t)}{E_0} = \frac{<\mathcal{A}^\star(t)\,\mathcal{A}(t)\,\mathbf{u}'_0, \mathbf{u}'_0>}{<\mathbf{u}'_0, \mathbf{u}'_0>}. \tag{5}$$

Thus, perturbations leading to the largest energy growth are the ones associated with the dominant eigenvalue of $\mathcal{A}^\star(t)\,\mathcal{A}(t)$ which is also the largest singular value of $\mathcal{A}(t)$. An optimal perturbation at the initial time is a right-singular vector associated with the largest singular value. To determine the operator $\mathcal{A}(t)$ (or its adjoint), we follow the method developed by Barkley et al. [30], the so-called time-stepper approach. The operator $\mathcal{A}(t)$ (or its adjoint) is first approximated by integrating forward (or backward) in time the linearized Navier-Stokes equations. Then, an Arnoldi algorithm based on a Krylov subspace constructed by successive applications of $\mathcal{A}^\star(t)\,\mathcal{A}(t)$ is used to extract the dominant singular values of $\mathcal{A}(t)$ for various time horizons. In the following, optimal disturbances of unit initial energy are referred to as optimal modes.

3 Results

3.1 Primary and secondary base flows

We first consider the primary base flow $\mathbf{U}_{2D}$. As explained in the previous section, in order to built the target velocity field for the fringe region. a preliminary computation has been carried out on a large domain capturing the upstream influence of the leading edges of the two plates. Figure 1(a) shows the streamwise evolution of the centerline velocity U_c. The result obtained by using the fringe region technique and the one associated with the finite-difference code are in perfect match. A similar observation can be made for integral boundary layers values (not shown here). It should be noted that for sections of interest ($x \leq x_0 = 16$), the flow is also similar to the one resulting from application of irrotational conditions in the entrance section and the potential effects due to geometry is negligible at this distance [31].

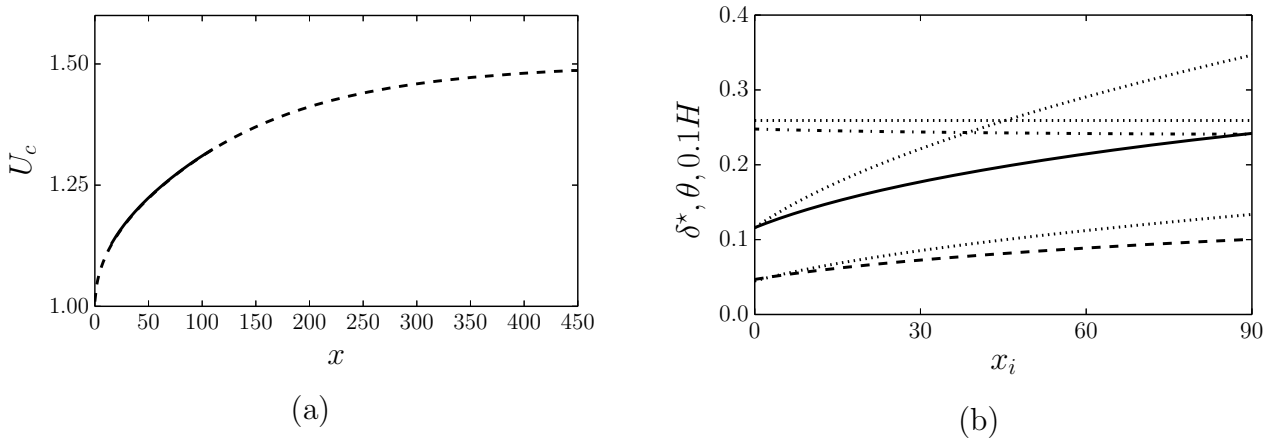

(a) (b)

Figure 1: Primary base flow $\mathbf{U}_{2D}$. (a) Velocity at the center of the channel. ——: DNS code with a fringe region technique. – – –: preliminary computation carried out with a finite-difference code of second order. (b) Integral boundary layer parameters: —— displacement thickness $\delta^\star$; – – –, momentum thickness θ; –·–· ,shape factor H;···, theoretical values for laminar Blasius profile (where $\delta^\star\,(x_i = 0)$ is fixed equal to the entrance channel flow value).

As previously mentionned, we note that the domain of interest is located well upstream of the fully-developed region (i.e. where $U_c = 1.5$). Defining the entrance length L_e as the streamwise position where U_c reaches 0.99% of the Poiseuille solution, there is a well-know criterion based on Blasius boundary-layer argument suggesting that $L_e/h \sim Re$, for large enough Re and thus quite a large extent for the flow developping zone. The data of Figure 1(a) give $L_e/h \approx 433$ which is very close to the value 442 obtained with the correlation proposed by [32].

In figure 1(b) we show the development of the displacement and momentum thickness ($\delta^\star$, θ, respectively) and the shape factor (i.e. $H = \delta^\star/\theta$), together with the well-known values for a zero-pressure gradient flat plate boundary layer. Due to the favorable pressure gradient, the boundary layers developing along the walls thicken slower than in flat plate case.

Let us now consider the secondary base flow $\mathbf{U}$. To generate streamwise-elongated streaks typical of the lift-up effect, a pair of streamwise vortices is injected in the section $x_i = 0$ of the boundary layer developing along the lower wall. The shape of the perturbation is obtained by solving the local, linear optimization problem, that is to say that the vortex pair maximizes kinetic energy in the framework of linear temporal stability analysis with parallel base flow assumption. Only one spanwise wavelength of the optimal (i.e. one vortex pair) is considered. Its numerical value is $\lambda_z \approx 1.14$. When rescaled by the displacement thickness at the inlet, the corresponding spanwise wavenumber ≈ 0.66 is very close to the value associated with a flat plate boundary layer without pressure gradient (≈ 0.65, see [33] for instance). The code used to compute the optimal vortex pair is detailed in Alizard et al. [34].

Different secondary base flows are computed for different amplitudes of the vortex pair at the section $x_i = 0$. In particular, we use the kinetic energy norm to measure amplitudes of initial streamwise vortices :

$$A_0 = \int_{-1}^{1} \left({v_s}^2\,(x_i = 0) + {w_s}^2\,(x_i = 0) \right)^{1/2} \mathrm{d}y,$$

with v_s and w_s being the normal and spanwise components of the primary disturbance. To

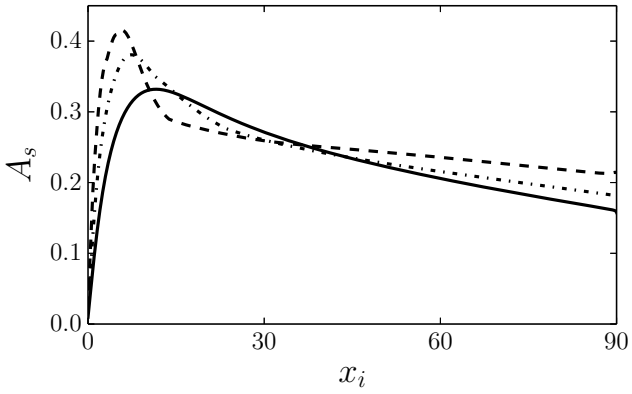

Figure 2: Secondary base flow $\mathbf{U}$. Streamwise evolution of the streak amplitude for $A_0 = 0.015$; ——, $A_0 = 0.025$ and - - -, $A_0 = 0.04$.

quantify the size of the streak at each streamwise position, we define its amplitude A_s as follows:

$$A_s(x) = \frac{1}{2U_c}\left[\max_{(y,z)}\left(U(x,y,z) - \overline{U}(x,y)\right) - \min_{(y,z)}\left(U(x,y,z) - \overline{U}(x,y)\right)\right],$$

where $\overline{U}$ is the z-average streamwise velocity and U_c the mean centerline velocity: $U_c = \overline{U}(x,0)$. The streamwise evolution of the streak amplitude is shown in figure 2 for the three increasing values $A_0 = 0.015$, 0.025 and 0.04. The maximum of amplitude observed during the transient growth process also increases, albeit more moderately, from 0.33 to 0.42, as an effect of nonlinear saturation. While for the lowest value the streak amplitude has rather smooth variations, for the higher value, we observe that the top of the profile is strongly pinched as it shifts upstream. For all flow cases, the three-dimensional flow evolves gradually into a quasi-parallel streaky motion further downstream. In figure 3, the streak is represented for the different initial amplitudes through streamwise velocity isocontour plots in the (y,z)-section where its amplitude is maximum. As observed by several authors for the case of a flat plate boundary layer, regions of strong spanwise shear are formed on both sides of the low-speed region which is also displaced further away from the wall, as the initial amplitude increases. For the largest value of A_0, non-linear effects are also responsible for shaping the low-speed streak into a typical mushroom pattern.

3.2 Local exponential secondary instability

In this section, we carry out a local modal stability analysis of the secondary base flow $\mathbf{U}$ for $A_0 = 0.015,\ 0.025$ and 0.04. For that purpose, we consider that $\mathbf{U}$ is invariant in the x direction (i.e. $\mathbf{U} = \mathbf{U}(y,z)$). A traveling wave is assumed for the secondary instability $\mathbf{u}'$ such as:

$$\mathbf{u}' = \hat{\mathbf{u}}(y,z)\, e^{i(\alpha x - \omega t)} + c.c, \tag{6}$$

where $\alpha \in \mathbb{R}$ is the streamwise wave number, $\omega \in \mathbb{C}$ is the complex circular frequency, and $c.c$ denotes the complex conjugate. We may decompose ω into a real part ω_r and an imaginary part ω_i, where the latter is the temporal amplification rate. A positive value of ω_i indicates the

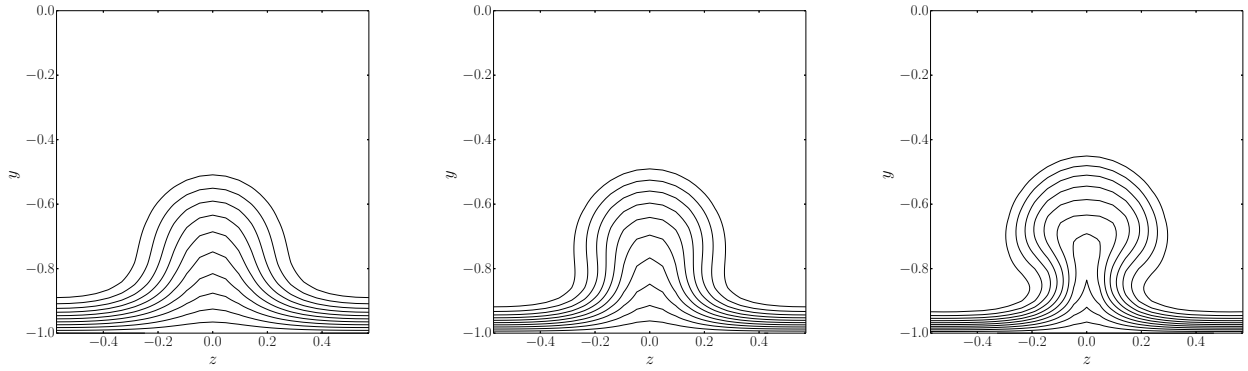

(a) (b) (c)

Figure 3: Secondary base flow **U**. Streamwise velocity contour plot in a (z, y) cross-stream plane at (a) $x_i = 11.7$, (b) $x_i = 7.4$ and (c) $x_i = 5.8$ for $A_0 = 0.015,\ 0.025$ and 0.04, respectively.

onset of an exponential growth mode. The linear system (2) reduces into a eigenvalue problem for ω. The code described in Alizard [35] is used to compute the least damped mode for various x_i-stations and α. In addition, we restrict our analysis to sinuous and varicose modes defined as:

$$\hat{u}(y,z) = -\hat{u}(y,-z),\ \hat{v}(y,z) = -\hat{v}(y,-z),\ \hat{w}(y,z) = \hat{w}(y,-z),$$

and

$$\hat{u}(y,z) = \hat{u}(y,-z),\ \hat{v}(y,z) = \hat{v}(y,-z),\ \hat{w}(y,z) = -\hat{w}(y,-z).$$

respectively.

In figure 4, we report results for $A_0 = 0.015,\ 0.025$ and 0.04. For the lowest streak amplitude, panel (a) shows that an exponentially growing mode exists for the sinuous case when $x_i > 6$. In addition, the temporal amplification rate reaches a maximum near $x_i \approx 20$ where $\omega_i \approx 0.28$. For the varicose symmetry, modes are seen temporally damped. The case $A_0 = 0.025$ is displayed in panels (c) and (d) for the sinuous and varicose symmetries, respectively. It shows that while the sinuous exponential mode is unstable for $x_i > 3.5$, the varicose wave is stable until $x_i \approx 7.5$. It exhibits for all streamwise positions a lower temporal amplification rate than the sinuous mode. In particular, ω_i reaches a maximum at $x_i \approx 10$ for the sinuous mode and $x_i \approx 20$ for the varicose mode where $\omega_i \approx 0.44$ and $\omega_i \approx 0.18$, respectively. Results for $A_0 = 0.04$ are shown in panels (e) and (f). The temporal amplification rate for the sinuous symmetry exhibits two peaks at $x_i \approx 5$ and $x_i \approx 12$ where $\omega_i \approx 0.48$ and ≈ 0.4, respectively. One may remark that the onset of several modes for large streak amplitudes have also recently been observed by John et al. [36] for the leading edge boundary layer near the attachment line. For the varicose case, ω_i peaks for $x_i \approx 12$ with a value ≈ 0.5. While the most amplified mode has a sinuous symmetry for $x_i < 8$, it exhibits a varicose pattern for larger streamwise position. The phase velocity $c = \omega_r/\alpha$ scaled by the maximum streamwise velocity $U_{\max} = \max_{y,z} U$ for $\max_\alpha \omega_i(\alpha, x_i)$ is shown in panel (b). The figure shows that both sinuous and varicose modes propagate with a phase velocity $0.7 < c/U_{\max} < 0.85$. It is interesting to notice that the onset of an exponentially growing mode is observed when $A_s \approx 30\%$ and $A_s \approx 38\%$ for the sinuous and varicose cases, respectively. These values are closed to the ones computed by Andersson

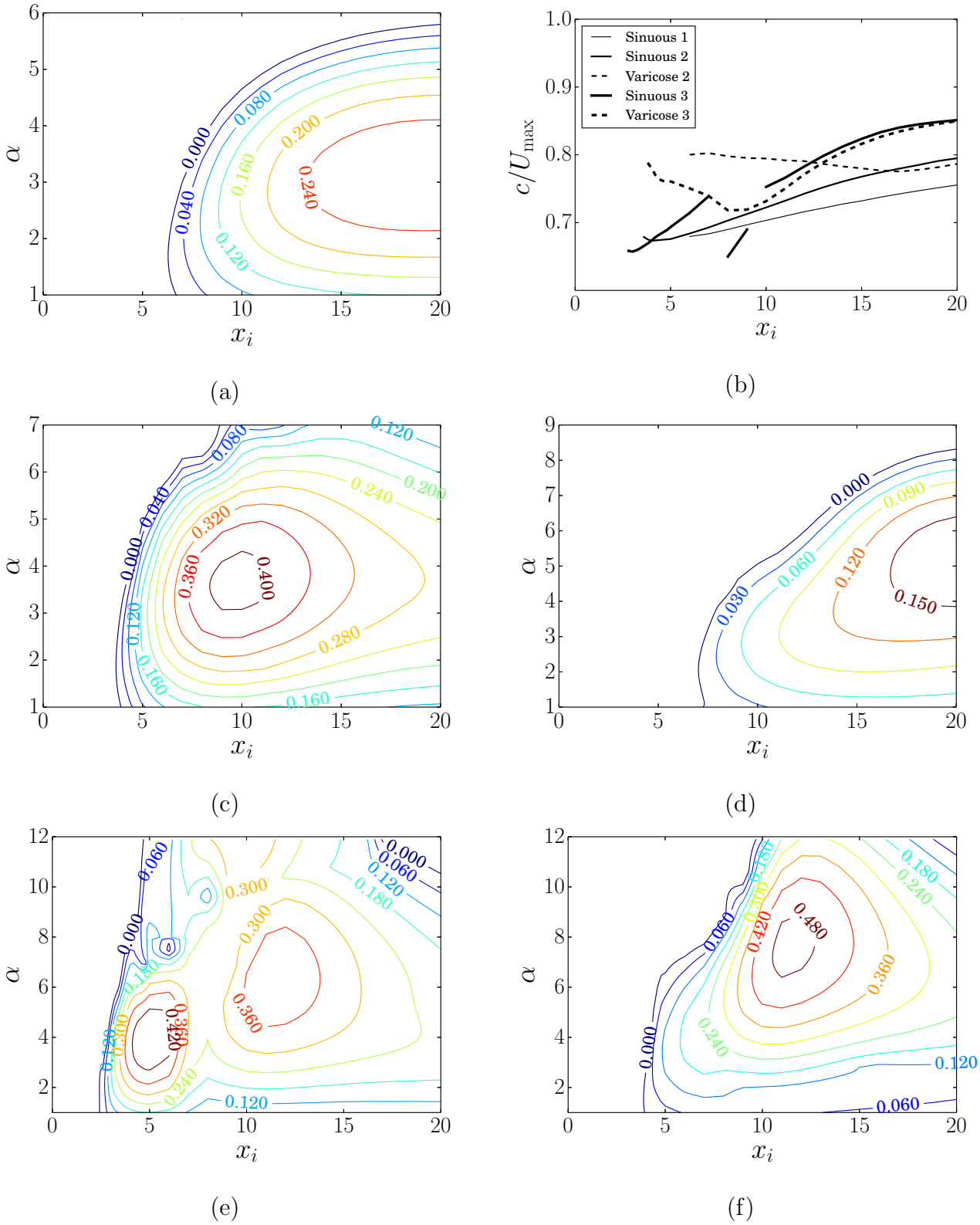

Figure 4: Secondary base flow **U**. Local stability analysis. Isocontours of the growth rate ω_i in the (α, ω_r) plane for $A_0 = 0.015$ (a), $A_0 = 0.025$ (c),(d) and $A_0 = 0.04$ (e),(f). The sinuous fundamental modes are shown in (a),(c) and (e). The fundamental varicose modes are shown in (c) and (d). Panel (b) Phase velocity $c = \omega_r/\alpha$ dimensionless by $U_{\max} = \max_{y,z} U(x, y, z)$ for $\max \omega_i$. Cases $A_0 = 0.015,\ 0.025$ and 0.04 are referenced as 1, 2 and 3, respectively.

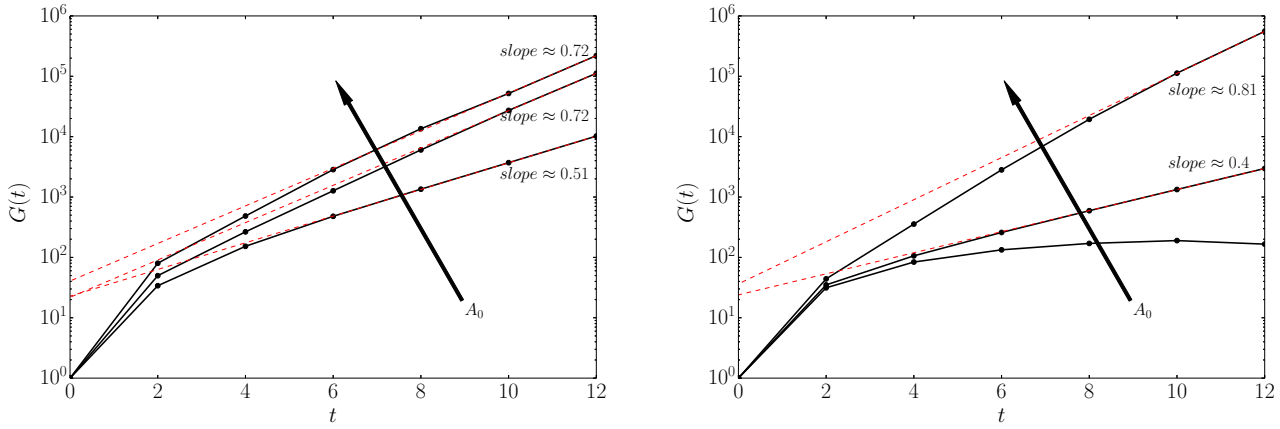

(a) (b)

Figure 5: Optimal energy gain as a function of the target time for $A_0 = 0.015$, 0.025 and $A_0 = 0.04$ with respect to (a) the sinuous symmetry and (b) the varicose symmetry. In red dashed lines, a least-square exponential fitting is also reported for $8 \leq t_{opt} \leq 12$.

et al. [11] for the case of a flat plate boundary layer (26% and 37%, respectively). Finally, the local stability analysis for the case $A_0 = 0.04$ is not able to predict which symmetry is selected by modal secondary disturbances. For the latter, temporal amplification rates reach similar values for both the varicose and sinuous case.

3.3 Global optimal perturbations: linear dynamics

3.3.1 Effect of streak amplitude and optimization time

Optimizations are carried out for secondary base flows illustrated in the previous section. In figure 5, we report the evolution of the optimal energy gain as a function of the target time for both sinuous and varicose symmetries. For all sinuous cases, optimization curves exhibit a strong amplification between $t_{opt} = 0$ and $t_{opt} = 2$ and is seen to grow almost exponentially with time after. It may suggest that optimal perturbations are subjected to a nonmodal amplification for short times and behaves as an exponential mode for long times. For the sinuous case, an exponential least square fit for $8 < t < 12$ provides exponential growth rates varying from 0.51 to 0.71 when A_0 is increased from 0.015 to 0.04. Recalling that $G(t)$ measures a kinetic energy, figure 5(a) shows that optimal sinuous modes exhibit an exponential behaviour for $t > 8$ with a temporal amplification rate $\sigma \approx 0.26$ for $A_0 = 0.015$ and $\sigma \approx 0.36$ for $A_0 = 0.025$ and 0.04. One may notice a close correspondence between amplification rates provided by the global optimization and modal local stability analysis especially for the lowest streak amplitude where nonparallelism effects are weaker (for instance $\max_{(\alpha,x_i)} \omega_i \approx 0.28$ for $A_0 = 0.015$). For the largest streak amplitude (i.e. $A_0 = 0.04$), global optimization suggests that local instability mode corresponding to the secondary peak observed in figure 4 (e) is selected for long times.

A similar behaviour is observed for the varicose case for $A_0 = 0.025$ and 0.04. Furthermore, the figure 5 shows that for $t_{opt} = 2$, optimal gains for varicose type reach levels of energy comparable to those of the sinuous one for all amplitudes that are considered. The figure also shows that while optimal disturbances have a sinuous symmetry for $A_0 = 0.015$ and 0.025, anti-

symmetric configuration is the most amplified for $A_0 = 0.04$. It is interesting to notice that such a behaviour is not well predicted by a local stability theory. In addition, for $A_0 = 0.015$ optimal energy gains with respect to varicose symmetry reach a maximum for $t_{opt} = 8$ and are seen to decrease for larger time horizons. It suggests that in this case, the varicose mode is not driven by an exponential instability. The latter remark is consistent with local stability results discussed in the previous section. For $t_{opt} = 4,\ 8$ and 12, we report time evolutions of $E(t)/E_0$ for optimal sinuous disturbances and $A_0 = 0.015$ in figure 6(a) and in figures 6 (b), (c) for the varicose type, where the amplitude is fixed to $A_0 = 0.015$ and 0.025, respectively. For the sinuous type, kinetic energy curves exhibit an algebraic growth for short times and an almost exponential behaviour for $t \geq 8$ for all initial conditions that are considered. In particular,

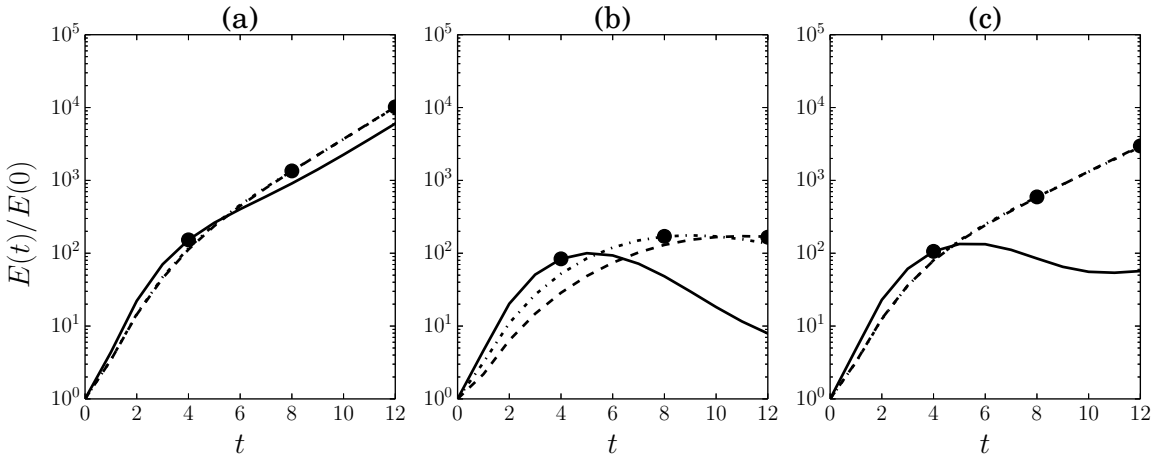

Figure 6: Kinetic energy amplification of disturbances as a function of time in the case of (a) sinuous symmetry and $A_0 = 0.015$; (b),(c) varicose symmetry for $A_0 = 0.015$ and $A_0 = 0.025$, respectively; for target times $t_{opt} = 4$ (——), $t_{opt} = 8$ (– – –) and $t_{opt} = 12$ (–·–·–). The optimal gains associated with $t_{opt} = 4,\ 8$ and 12 are also indicated by •.

kinetic energy curves are superimposed for $t_{opt} = 8$ and 12.

To firstly characterize optimal perturbations in terms of optimization times and streak amplitudes, we introduce a measure of its streamwise localization such as

$$E_x(x_i, t) = \int_{L_y} \int_{L_z} (\mathbf{u}' \cdot \mathbf{u}')(x_i, y, z, t)\, \mathrm{d}y \mathrm{d}z.$$

As shown in figures 7 and 8, optimal disturbances for both the varicose and sinuous cases are seen to be localized in the streamwise direction whereas optimal modes for wall-bounded flows without streaks are dominated by infinitely elongated structures [33]. In the case of the primary base flow for the entrance channel flow, optimal disturbances computed with a similar method yield to strongly elongated streaks similarly as the ones obtained by Monokrousos et al. [37] for a flat plate boundary layer.

Optimal sinuous and varicose modes are seen to propagate downstream as they gain in kinetic energy. The latter behavior is expected due to the convective nature of streaks as reported for the flat plate boundary layer by Brandt et al. [29]. For the sinuous symmetry, distributions of E_x for $t = 0$ and $t = t_{opt}$ are shown in figure 7 as a function of the distance

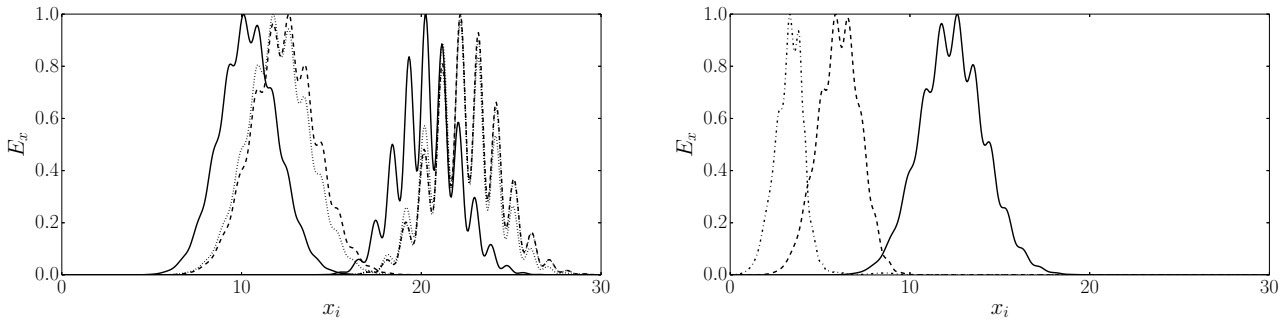

Figure 7: Sinuous case. (a) $A_0 = 0.015$. Distribution of E_x as a function of the streamwise position for $t_{opt} = 4$ (——), $t_{opt} = 8$ (– – –) and $t_{opt} = 12$ (...) at $t = 0$ and $t = 12$. (b) $t_{opt} = 12$. Distribution of E_x for the optimal perturbation as a function of the streamwise position for $A_0 = 0.015$ (——), $A_0 = 0.025$ (– – –) and $A_0 = 0.04$ (...) at $t = 0$. E_x is normalized by its maximum for all cases.

from the inlet. For all amplitudes, the figure shows that for $t_{opt} = 4,\ 8$ and 12 optimal modes starts to be amplified close to the streamwise position where local stability theory predicts the onset of an exponentially sinuous growing mode. Consistent with results shown in figure 6 (a), the spatial support of optimal mode for $t_{opt} = 8$ remains coincident with the one for $t_{opt} = 12$ between $t = 0$ and $t = 12$. The envelope of the optimal perturbation is seen to be unchanged for larger t_{opt} (not shown here for the sake of conciseness). When considering the effect of A_0, the figure 7 (b) shows that as the streak amplitude increases, the optimal mode tends to be shifted upstream and exhibits a narrow envelope in the streamwise direction.

For the varicose symmetry, when $A_0 = 0.015$ an algebraic growth dominates for all times. In particular, the distribution of the optimal energy gain as a function of the target time exhibits a concave shape (see figure 5(b)). For a longer optimization time ($t_{opt} > 10$) the optimal kinetic energy gain tends to decrease. This behaviour is also observed through kinetic energy curves shown in figure 6 (b). It is consistent with results provided by local stability analyses indicating that the flow is temporally stable at all streamwise positions. When the amplitude is increased up to $A_0 = 0.025$, we observe that the growth is due to a transient mechanism for short optimization time. In particular, the kinetic energy curve for $t_{opt} = 4$ (and also below) exhibits a bump whereas for $t_{opt} = 8$ and 12 (and also above), the increase in kinetic energy is due to the combined effect of an algebraic short time mechanism and a quasi-exponential growth (see figure 6 (c)). This can be explained by the fact that the spatial distribution of the latter optimal modes are located in different regions. As shown in figure 8, while the optimal mode that maximizes kinetic energy for $t_{opt} = 4$ is located in the upper part of the streaky base flow at the initial time, the one associated with $t_{opt} = 12$ is located far downstream. In particular, at the initial time, optimal mode for $t_{opt} \geq 6$ exhibits a spatial distribution mainly concentrated upon the streamwise position where local stability theory predicts the onset of an unstable exponential varicose mode whereas optimal mode for $t_{opt} \leq 4$ gets amplified in a convectively stable region.

For sinuous cases, $E_x(x_i, t)$ is not too affected by time optimization as shown in figure 7. A similar behaviour is also observed for $A_0 = 0.04$ (not shown here).

Hereafter, we will consider representative varicose and sinuous perturbations that are defined

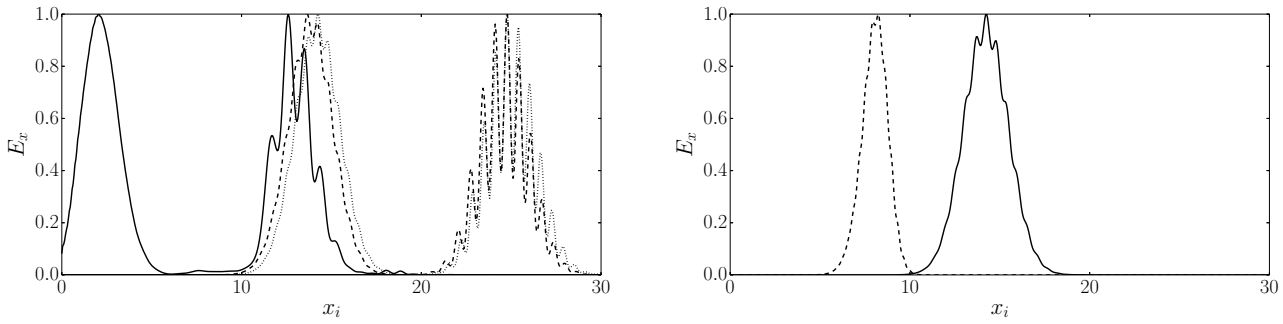

Figure 8: Varicose case. (a) $A_0 = 0.025$. Distribution of E_x as a function of the streamwise position for $t_{opt} = 4$ (——), $t_{opt} = 8$ (– – –) and $t_{opt} = 12$ (...) at $t = 0$ and $t = 12$. (b) $t_{opt} = 12$. Distribution of E_x for the optimal mode as a function of the streamwise position for $A_0 = 0.025$ (——) and $A_0 = 0.04$ (– – –) at $t = 0$. E_x is normalized by its maximum for all cases.

Mode	Symmetry	t_{opt}	A_0
V_{11}	Varicose	2	0.015
V_{12}	Varicose	2	0.025
V_{22}	Varicose	12	0.025
S	Sinuous	12	0.025

Table 2: Representative optimal modes for sinuous and varicose symmetries.

in table 2. V_{11}, V_{12} and V_{22} are associated with mostly amplified varicose perturbations for short and large optimization times, respectively. Considering the weaker effect of t_{opt} on the sinuous case, only a single mode is considered for $A_0 = 0.025$, noted S.

3.3.2 Linear space-time dynamics and amplification mechanisms

In this section, we will analyze the linear space-time dynamics for optimal wavepackets associated with varicose and sinuous symmetries. To this end, we consider two varicose modes, obtained for $A_0 = 0.025$, $t_{opt} = 2$ and $t_{opt} = 12$ (i.e. V_{12} and V_{22}, respectively); and the sinuous optimal mode for the same amplitude and the target time $t_{opt} = 12$: S. Let us first investigate the V_{12} case. In figure 9, we show the streamwise vorticity, spanwise vorticity and the streamwise velocity components of the perturbation for time varying from $t = 0$ to $t = 3$. The optimal mode takes the form of a wavepacket localized upstream at the initial time. For such a time, the perturbation is inclined in the upstream direction and is composed of both wall-normal and spanwise vorticity components, mainly localized in the flanks of the low-speed streak. Then, as time evolves the mode is reoriented along the wall-normal shear direction where the streamwise component gets amplified and is elongated in the streamwise direction. For times shown in figure 9, wavepacket is localized in a region where local stability theory predicts that exponential modes are damped temporally. From above discussion, figure 9 suggests a combined effect due to Orr and lift-up mechanisms for the growth of initial disturbances. To gain further insight into these amplification mechanisms, we analyze hereafter the different terms involved in the time evolution of the integrated kinetic energy of disturbances. For that purpose, we introduce

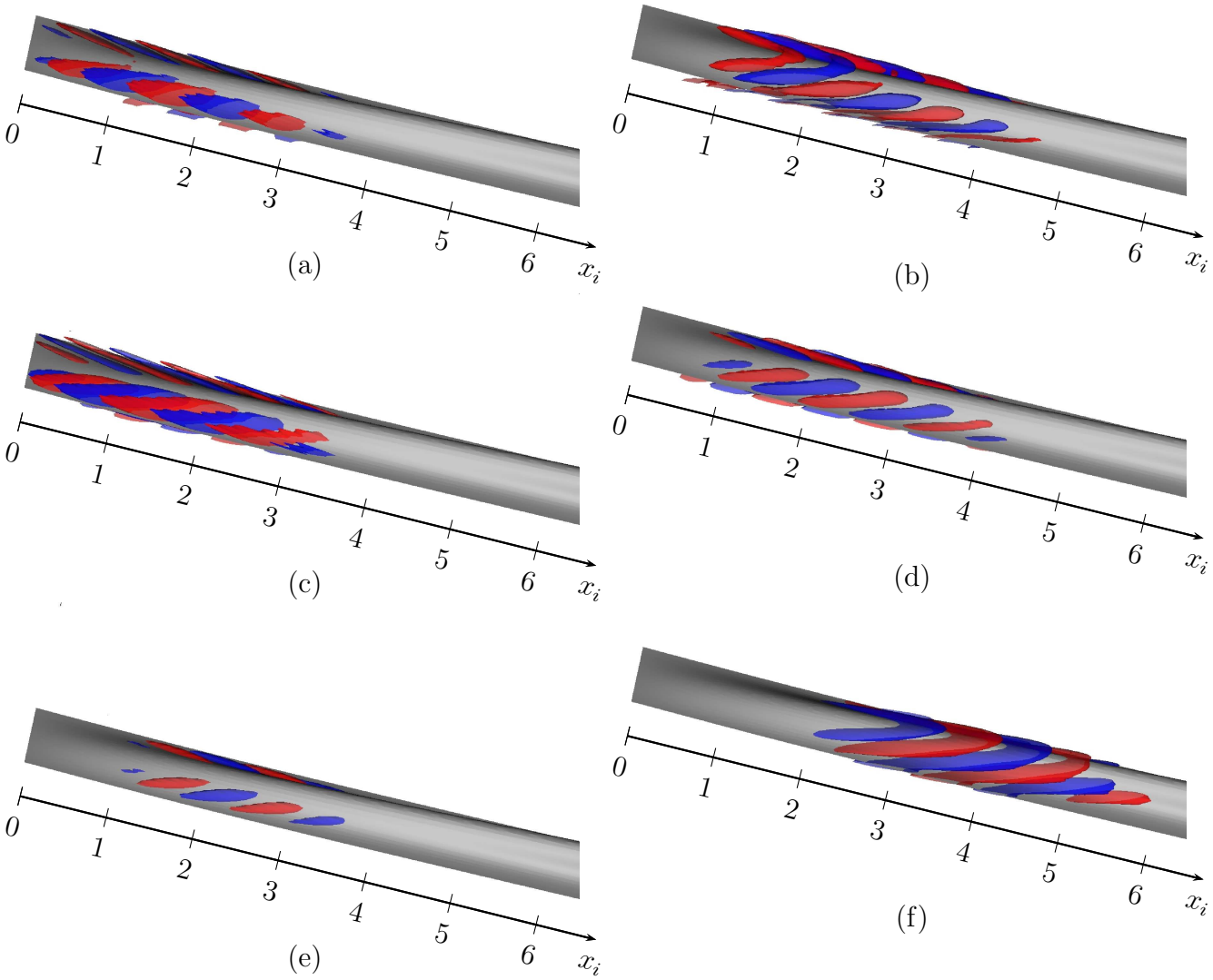

Figure 9: Varicose case V_{12}. The $L2$ norm of the perturbation is fixed equal to unity at $t = 0$. Isosurfaces of spanwise and streamwise perturbation vorticity components are shown in panels (a),(b) and (c),(d), respectively for times $t = 0$ ((a) and (c))and $t = 1$ ((b) and (d)). Surface levels correspond to ± 500. Isosurfaces of the streamwise perturbation velocity component is shown in panels (e) and (f) for $t = 1$ and $t = 3$. Surface levels correspond to $+/-100$. The surface level 0.7 for the streamwise component of the base flow is represented in gray for all panels.

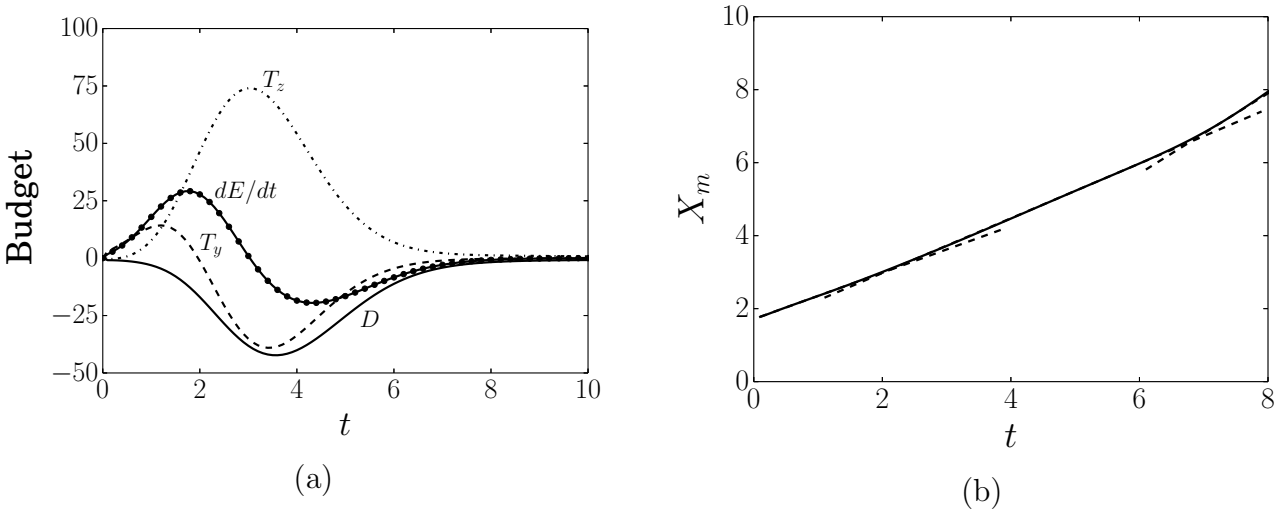

(a) (b)

Figure 10: Varicose case V_{12}. (a) Time evolution of the kinetic energy budget. (b) Time evolution of the barycenter position. In dashed lines, a linear regression is used to fit the curve for three space intervals. The velocity varies from 0.63, 0.75 to 1.1.

the so-called Reynolds-Orr equation:

$$\frac{dE}{dt} = -\int_D (\mathbf{u}' \cdot \nabla \mathbf{U}) \cdot \mathbf{u}' \, \mathrm{d}D - \frac{1}{Re} \int_D \nabla \mathbf{u}' : {}^t\nabla \mathbf{u}' \, \mathrm{d}D \tag{7}$$

where : represents the double dot product operator and D the computational box. The first term on the right-hand side are production terms associated with interactions with the mean shear and the second term is the dissipation due to viscous effects, respectively. In particular, we note hereafter $T_y = -\int_D u'v' \partial U/\partial y \, \mathrm{d}D$, $T_z = -\int_D u'w' \partial U/\partial z \, \mathrm{d}D$ the production terms associated with the work of the Reynolds stresses against, respectively, the wall-normal shear $\partial U/\partial y$ and spanwise shear $\partial U/\partial z$. The time evolution of contributions to the kinetic energy budget for V_{12} is reported in figure 10(a). We also report in figure 10(b) the time evolution of the wavepacket barycenter defined as:

$$X_m(t) = \frac{\sum_i \gamma[i](t) \, X[i]}{\sum_i \gamma[i](t)},$$

where i indicates the grid-point in the streamwise direction, $\gamma[i]$ and $X[i]$ represent the integrated kinetic energy over the cross-section (y z) and the corresponding streamwise position, respectively. Figure 10(a) shows that production terms T_y and T_z contribute mainly to the growth, the other ones can be thus considered as negligible. As reported in figure 10(b), the wavepacket is concentrated near the inlet, above the onset of a varicose exponentially growing mode, and propagates with a low velocity $\approx 0.6\ U_c$ for $t < 4$. This velocity is substantially lower than the velocity speed of modal secondary varicose instability given by local stability analysis carried out in section 3.2. We may also remark that the wavepacket is localized in a region where the base flow varies significantly along the streamwise direction (see figure 2). The production term associated with the wall normal shear of the basic flow is positive until $t = 2$ and then becomes negative. We also note that the production term that corresponds to

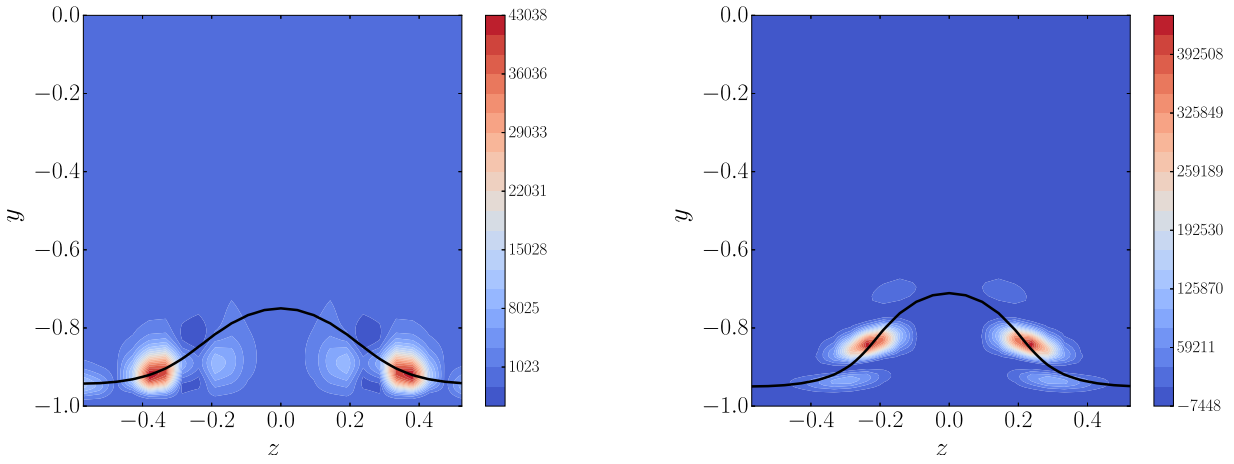

Figure 11: Varicose case V_{12}. Cross-sections of production terms (a) T_y at $t = 1.2$ for $x_i = X_m\,(t = 1.2) \approx 2.7$ and (b) T_z at $t = 3$ for $x_i = X_m(t = 3) \approx 3.7$. Full line represents position where $U = 0.7$.

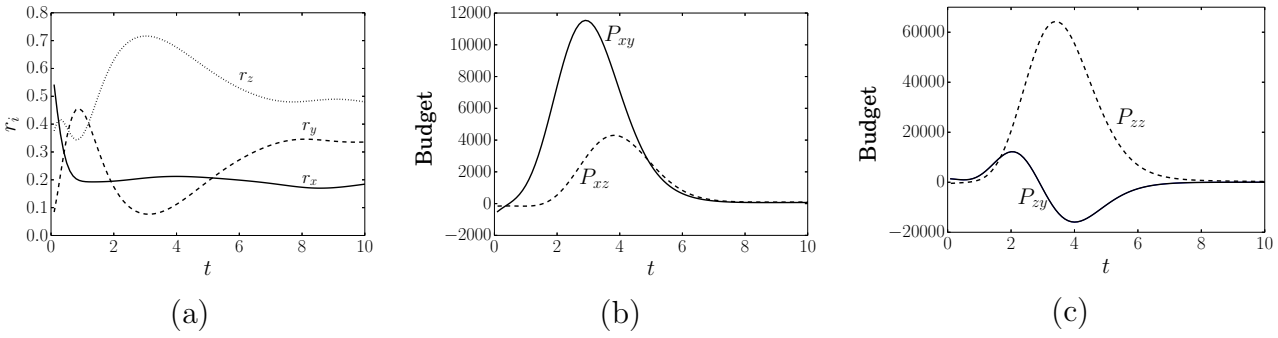

Figure 12: Varicose case V_{12}. (a) Time evolution of r_x, r_y and r_z. Vorticity budget for Ω'_x (b) and Ω'_z (c).

the work of the Reynolds stress against the spanwise shear is dominant for times greater than 1. This is somewhat unexpected, since it is well accepted that varicose perturbations are driven by the action of the wall-normal basic shear (see Cossu and Brandt [38] for instance). Such a behaviour is also observed by Hoepffner et al. [19] using a local optimal mode analysis for a streaky boundary layer flow and by Cherubini et al. [23] for a flow behind a roughness element using a global optimal mode theory. In figure 11, we show cross-sections of T_y and T_z at $t = 1.2$ and $t = 3$, respectively, where production terms peak. The streamwise positions of extracted planes are fixed to the barycenter position for these times. From figure 11, we may observe that production terms (both T_y and T_z) are mainly localized on the flanks of the low-speed streak, consistent with the spatial distribution of the optimal mode shown in figure 9.

To get a better understanding of the underlying mechanisms, we investigate the time evolution of the enstrophy ratios, defined as:

$$r_i = \frac{\Omega'_i}{\sum_j \Omega'_j} \text{ with } \Omega'_i = \int_D \omega_i'^2 \mathrm{d}D \text{ and for } i = x, y, z, \tag{8}$$

where $\omega' = \nabla \times \mathbf{u}'$ is the perturbation vorticity vector. A similar analysis is conducted by Schmidt et al. [39] to understand the physical mechanisms associated with optimal wavepackets growing in a corner flow. At the initial time, the perturbation is mainly composed of spanwise and streamwise vorticity components as shown in figure 12(a). For early times, we observe an increase in the contribution of the wall normal vorticity component. In addition, the spanwise vorticity contribution is almost keep constant during this stage which is associated with the Orr-mechanism observed in figure 11. For $t > 1$, a strong increase of the spanwise vorticity contribution is observed. While the increase of r_y may be attributed to a lift-up mechanism whereby vorticity is transferred from the streamwise to the wall-normal direction, the understanding of r_z increasing requires further analysis. To this end, we introduce the streamwise, wall-normal and spanwise vorticity perturbation transport equations such as:

$$\frac{d\omega'_x}{dt} \approx \frac{\partial U}{\partial z}\frac{\partial v'}{\partial x} - \frac{\partial U}{\partial y}\frac{\partial w'}{\partial x} - \frac{1}{Re}\Delta\omega'_x; \tag{9}$$

$$\frac{d\omega'_y}{dt} \approx \frac{\partial U}{\partial z}\frac{\partial v'}{\partial y} - \frac{\partial U}{\partial y}\frac{\partial v'}{\partial z} - \frac{1}{Re}\Delta\omega'_y; \tag{10}$$

$$\frac{d\omega'_z}{dt} \approx \frac{\partial U}{\partial z}\frac{\partial w'}{\partial y} - \frac{\partial U}{\partial y}\frac{\partial w'}{\partial z} - \frac{1}{Re}\Delta\omega'_z. \tag{11}$$

where we neglect terms associated with gradients of wall-normal and spanwise components of the secondary base flow. Multiplying both sides of equation (9) by ω'_x and integrating over the whole domain yield to:

$$\frac{d\Omega'_x}{dt} \approx \underbrace{\int_D \frac{\partial U}{\partial z}\frac{\partial v'}{\partial x}\omega'_x \mathrm{d}D}_{P_{xz}} \underbrace{- \int_D \frac{\partial U}{\partial y}\frac{\partial w'}{\partial x}\omega'_x \mathrm{d}D}_{P_{xy}} \underbrace{- \frac{1}{Re}\Delta\Omega'_x}_{D_x}, \tag{12}$$

where P_{xz} is associated with the tilting of $\partial v'/\partial x$ by the spanwise shear and P_{xy} is a production term due to the tilting of $\partial w'/\partial x$ by the wall-normal shear; D_x is a viscous dissipation term. For the transport of Ω'_y, we have

$$\frac{d\Omega'_y}{dt} \approx \underbrace{\int_D \frac{\partial U}{\partial z}\frac{\partial v'}{\partial y}\omega_y \mathrm{d}D}_{P_{yz}} \underbrace{- \int_D \frac{\partial U}{\partial y}\frac{\partial v'}{\partial z}\omega'_y \mathrm{d}D}_{P_{yy}} \underbrace{- \frac{1}{Re}\Delta\Omega'_y}_{D_y}, \tag{13}$$

where P_{yz} is a vortex-stretching term due to the spanwise shear and P_{xy} is a production term due to the tilting of $\partial v'/\partial y$ by the wall-normal shear; D_y is a viscous dissipation term. Similarly, we obtain for Ω'_z:

$$\frac{d\Omega'_z}{dt} \approx \underbrace{\int_D \frac{\partial U}{\partial z}\frac{\partial w'}{\partial y}\omega'_z \mathrm{d}D}_{P_{zz}} \underbrace{- \int_D \frac{\partial U}{\partial y}\frac{\partial w'}{\partial z}\omega'_z \mathrm{d}D}_{P_{zy}} \underbrace{- \frac{1}{Re}\Delta\Omega'_z}_{D_z}, \tag{14}$$

where P_{zz} is a vortex-stretching term due to the spanwise shear and P_{zy} is a vortex-tilting production term associated with by the wall-normal shear; D_z is a viscous dissipation term.

The figure 12(b) shows that the transient mechanism gives rise to a positive production term for the streamwise vorticity for $t > 1$. The latter is mainly due to the wall normal shear,

as also found by Brandt and de Lange [17] for the symmetric breakdown of the streak by DNS for a flat plate boundary layer. In figure 12(c), we show P_{zy} and P_{zz} as a function of time. As it can be seen, production terms reach an higher level than their streamwise vorticity counterparts. One may also notice that for $t < 2$ the production term is slightly dominated by P_{zy} before to be temporally damped. For larger times, the figure shows that production terms are mainly driven by P_{zz}. While the behaviour of P_{zy} is due to a stretching of the perturbation that rotates around the $z-$axis under the action of the Orr-mechanism, P_{zz} can be associated with the lift-up mechanism due to the spanwise shear. The mean wall-normal vorticity is tilted into the $z-$direction by the perturbation strain rate $\partial w'/\partial y$, giving rise to the increase of spanwise vorticity. It is classically admitted that for three-dimensional perturbations transient mechanisms are associated with the combined effect of an Orr and lift-up mechanism as well detailed in Butler and Farrell [40]. However, the latter authors consider only a base flow with a wall normal shear. In this case, the combined effect of Orr and lift-up mechanisms is due to both the wall-normal and spanwise shear of the base flow. Furthermore, the similarities between figure 10 (a) and 12 (b) give strong indications that the kinetic energy is mainly driven by the spanwise vorticity production term identified above. Finally, for times larger than 6 the flow relaxes to an equilibrium state suggesting that the flow is driven by a modal mechanism for these times (see figure 12(a)).

For V_{22}, we report in figure 13 (a)-(d), the spanwise and streamwise vorticity components for this mode at $t = 0$ and $t = 2$. It can be seen that the optimal mode takes the form of a wavepacket that is localized downstream where local stability theory predicts the onset of a varicose exponential growing mode (see figure 4 (c)). The figures show that while V_{12} is mostly concentrated in the flanks of the low-speed streak, V_{22} is strongly localized on its head as also identified through its streamwise component in figure 13 (c) and (d). In addition, V_{22} extends in the streamwise direction on a larger distance than V_{12}. As for V_{12}, V_{22} is initially inclined against the mean shear and is reoriented along the streamwise direction while being convected downstream. Finally, one may also observe from figures 13(c) and (d), that the streamwise component increases significantly less with time in comparison with V_{12}. To give further insight about mechanisms that are responsible for the growth, we report in figure 14 (a), the kinetic energy budget for V_{22}. The figure shows that while both spanwise and wall normal shear contribute to an increase in kinetic energy for V_{12}, the production is only driven by T_y for V_{22}. In figure 14(b), we also report the time evolution of its barycenter. It shows that V_{22} travels with a group velocity $\approx 0.8\ U_c$ which confirms that the mode is convected downstream by the outer region of the boundary layer associated with the lower wall.

Figure 15 displays cross-sections of the dominant production term T_y for $t = 3$ and $t = 5$ at $x_i = X_m\,(t = 3)$ and $x_i = X_m(t = 5)$, respectively. We also report the position of the inflection point associated with the low speed streak and the velocity contour where $U = \mathrm{d}X_m/\mathrm{d}t$. The figure shows that the production term T_y is mainly localized around the inflection point. This characteristics is observed for times $t > 3$.

In figure 16 (a), we report the temporal evolutions of the normalized perturbation enstrophy ratios for V_{22}. In figures 16(b) and (c), production terms associated with streamwise and spanwise vorticity components are displayed. The figure 16 (a) shows that the initial solution predominantly consists of streamwise and spanwise vorticity. During the initial stage of transient amplification, a part of the vorticity is transferred from the streamwise to the wall normal component. The underlying evolution is characteristic of the lift-up mechanism associated with

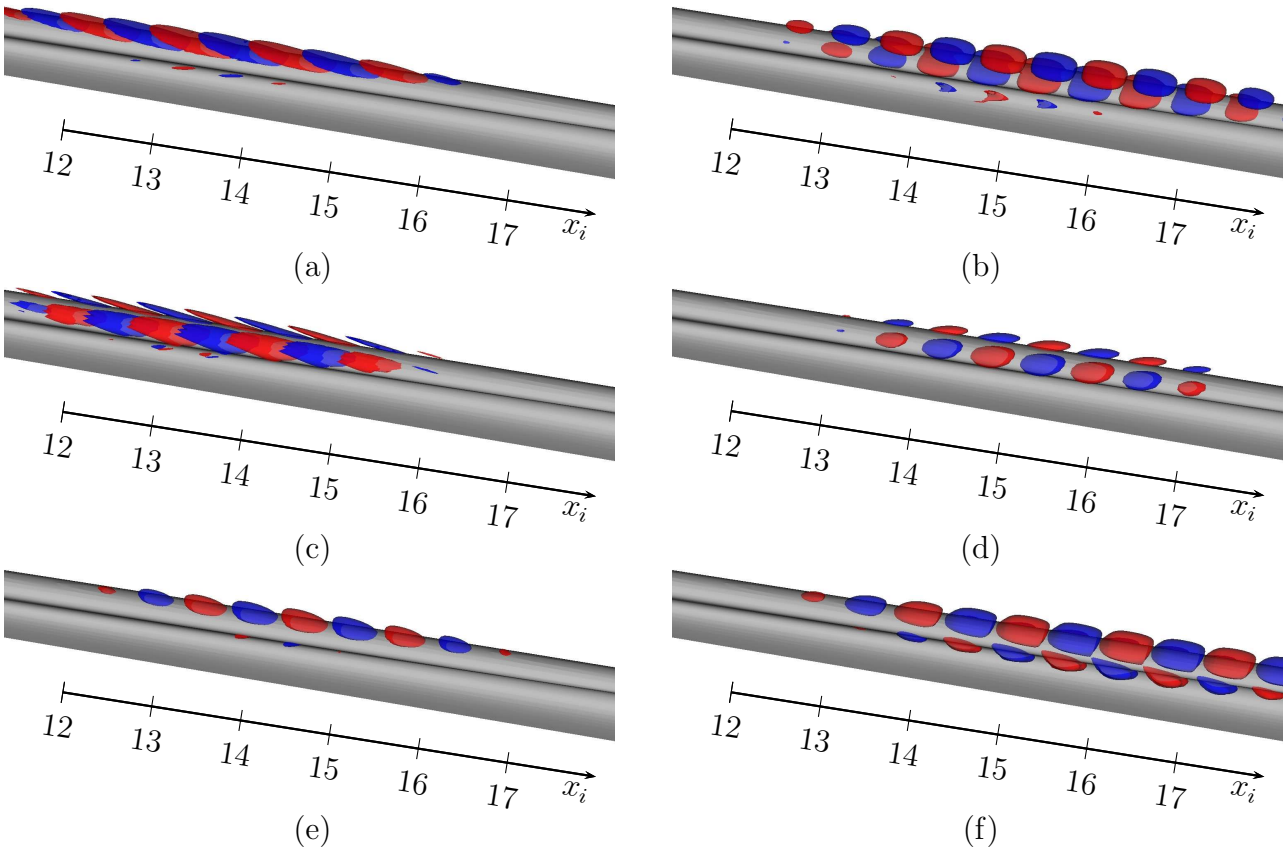

Figure 13: Varicose case V_{22}. The $L2$ norm of the perturbation is fixed equal to unity at $t = 0$. Isosurfaces of spanwise and streamwise perturbation vorticity components are shown in panels (a),(b) and (c),(d), respectively for times $t = 0$ ((a) and (c))and $t = 1$ ((b) and (d)). Surface levels correspond to ± 500. Isosurfaces of the streamwise perturbation velocity component is shown in panels (e) and (f) for $t = 1$ and $t = 3$. Surface levels correspond to ± 100. The surface level 0.8 for the streamwise component of the base flow is represented in gray for all panels.

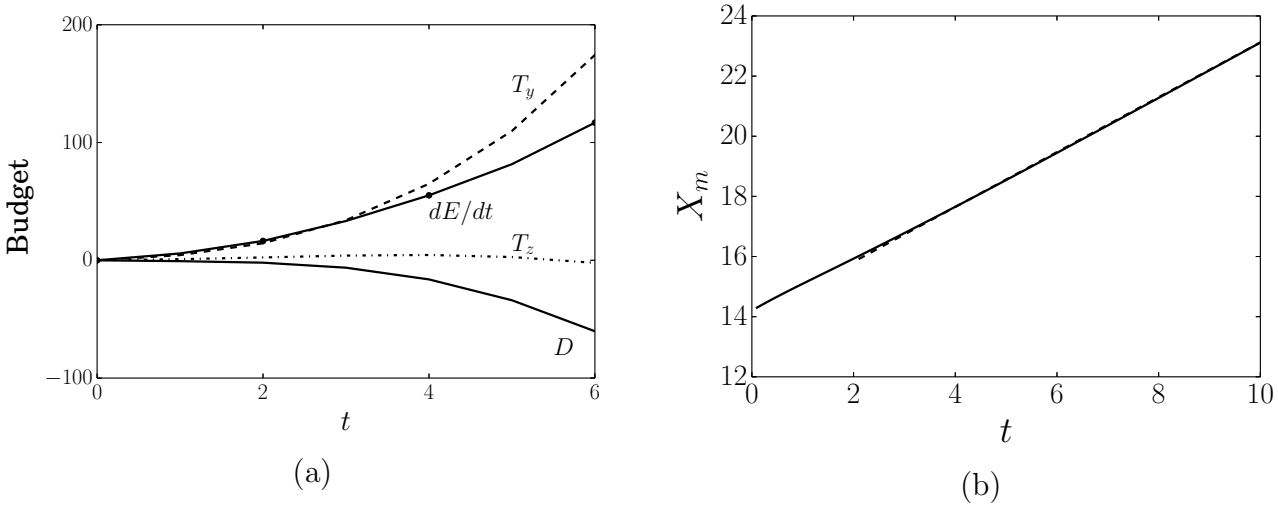

Figure 14: Optimal mode V_{22}. (a) Time evolution of kinetic energy budget. (b) Time evolution of barycenter position. $dX_m/dt \approx 0.9$ (in dashed-line).

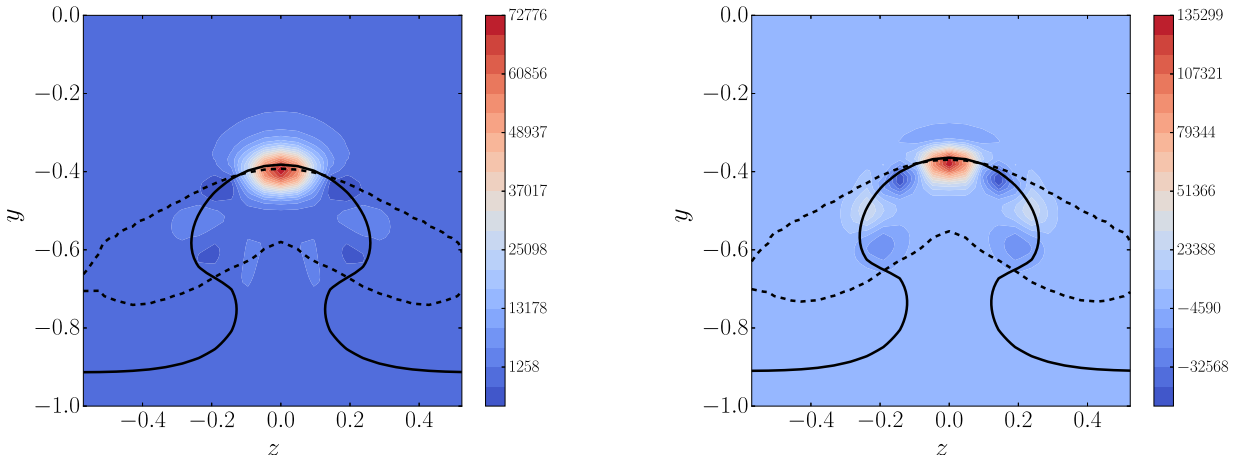

Figure 15: Varicose case V_{22}. Production terms T_y at $t = 3$ (a) and $t = 5$ (b) for $x_i = X_m\,(t = 3) = 16.8$ and $x_i = X_m\,(t = 5) = 18.5$, respectively. Full line represents the position where $U = dX_m/dt$. Dashed-lines represent positions of wall-normal inflection points.

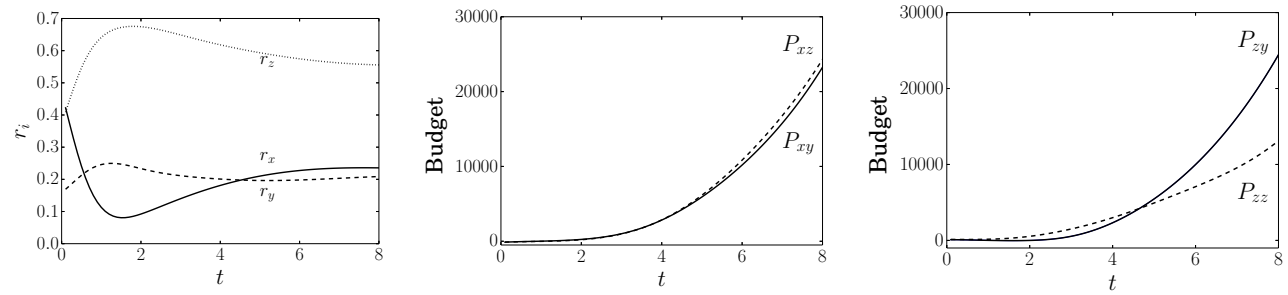

Figure 16: Varicose case V_{22}. (a) Time evolution of r_x, r_y and r_z. Vorticity budget for Ω'_x (b) and Ω'_z (c).

the wall normal shear. We also observe in figure 16 (c) that a part of streamwise vorticity is transferred to the spanwise component. During this preliminary stage the tilting term (i.e due to the spanwise shear) is dominant. However, the contribution to the kinetic energy budget of the production associated with the spanwise shear is negligible, in contrast to its important role in the increase of kinetic energy for V_{12}. Hence, the mechanism responsible for the growth is seen to be associated with a combination of Orr/lift-up mechanism due to the wall-normal shear for early times, the mechanism is rapidly overtaken by an exponential mode due to a point of inflection along the wall-normal direction in the outer part of the boundary layer. In particular, V_{22} for times greater than 3 exhibits close similarities with the outer mode described by Vaughan and Zaki [15] for the flat plate boundary layer case. It confirms that V_{22} is governed by an exponential mode for large times having close correspondence with results provided by local stability theory. Finally, one may also observe that $t > 5$ an equilibrium state is reached for enstrophy ratios (see figure 16 (a)) and the production of its streamwise components is governed by both the wall-normal and spanwise shear.

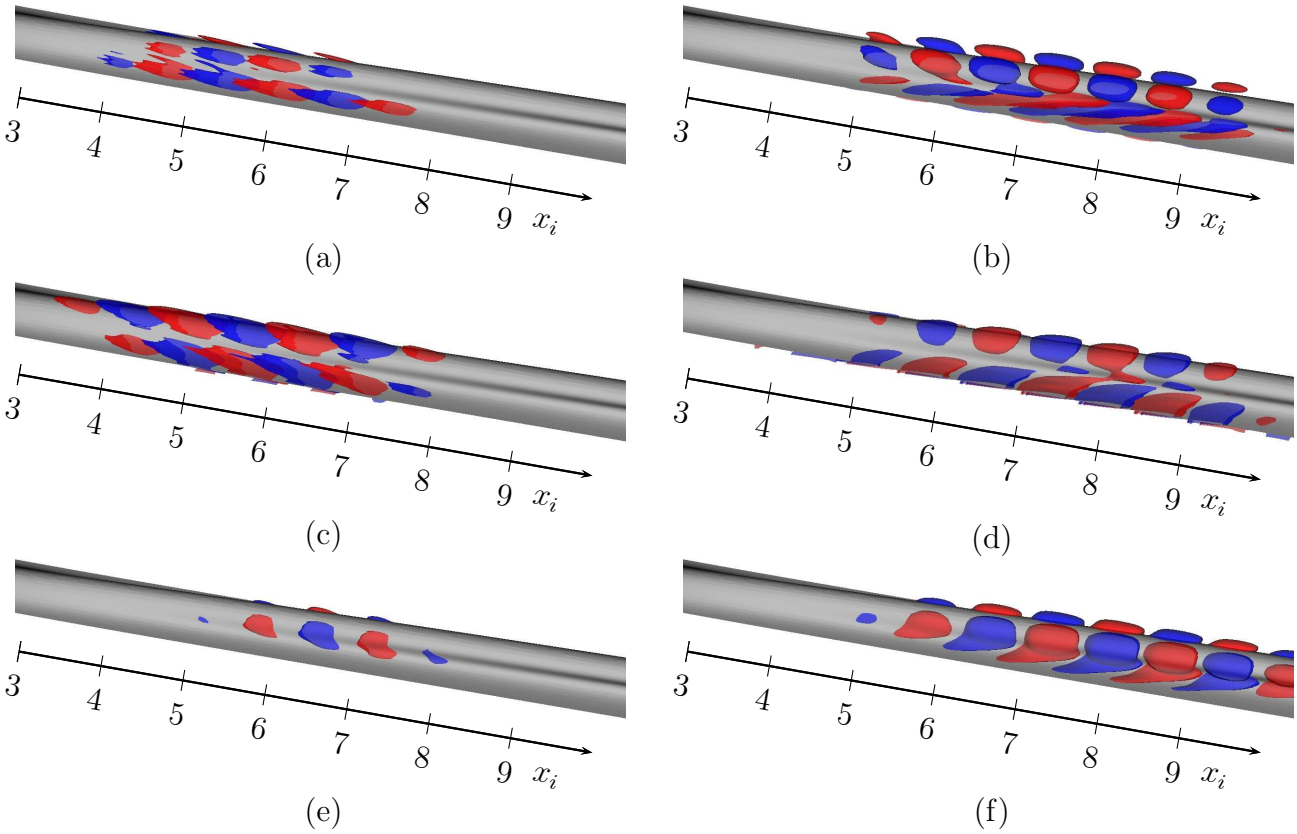

Figure 17: Sinuous case S. The $L2$ norm of the perturbation is fixed equal to unity at $t = 0$. Isosurfaces of spanwise and streamwise perturbation vorticity components are shown in panels (a),(b) and (c),(d), respectively for times $t = 0$ ((a) and (c))and $t = 2$ ((b) and (d)). Surface levels correspond to $+/-300$. Isosurfaces of the streamwise perturbation velocity component is shown in panels (e) and (f) for $t = 1$ and $t = 4$. Surface levels correspond to $+/-100$. The surface level 0.8 for the streamwise component of the base flow is represented in gray for all panels.

The secondary instability of streaks with respect to S is illustrated in figure 17 where streamwise, spanwise vorticity and streamwise velocity components are shown at various times. The optimal mode takes the form of a wavepacket where its distribution at the initial time exhibits both spanwise and streamwise vorticity. S is localized on both the flanks of the low speed streak and outside in the boundary layer. It is inclined in the upstream direction at $t = 0$ and is reoriented downstream for larger time while its streamwise component is increasing. Hence, it also suggests for short times, a combined effect of Orr/lift-up mechanism.

The kinetic energy budget is displayed in figure 18 (a). The figure shows that as it can be expected for sinuous configuration the main contributor to the energy amplification is the spanwise production term T_z, even for early times. In figure 18 (b), the space-time evolution of the barycenter shows that the optimal mode travels with a velocity group $\approx 0.8\ U_c$ which is consistent with findings of Andersson et al. [11] found in a local framework.

The production term T_z is shown in the cross-stream plane at $t = 3$ and $t = 5$ for $x_i = X_m(t = 3)$ and $x_i = X_m(t = 5)$, respectively. The figure shows that for t greater than 3, the optimal mode is dominated by an inviscid mechanism associated with points of inflection along

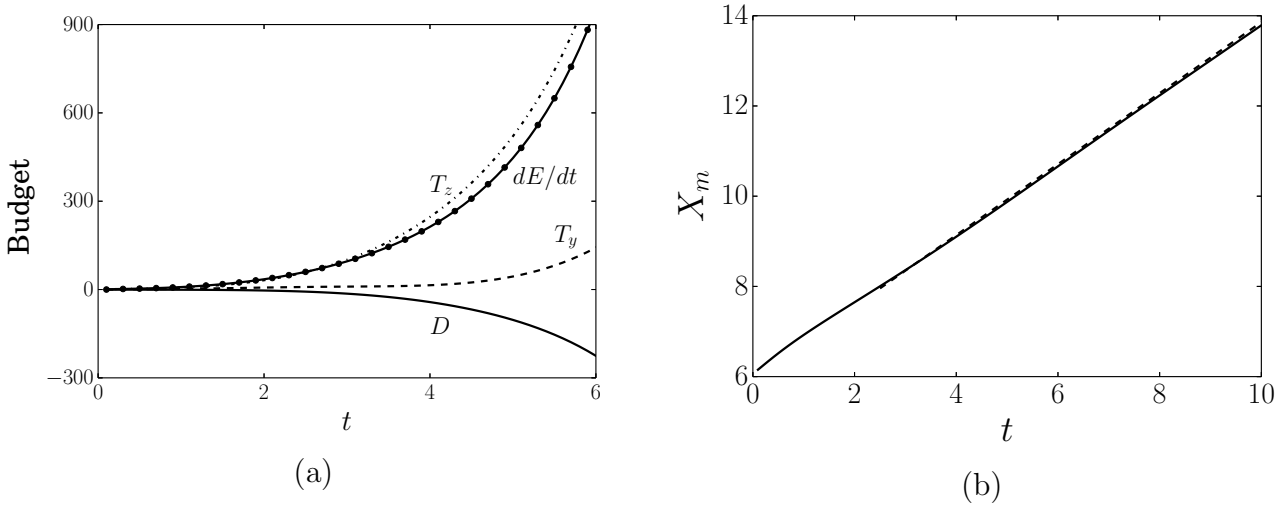

Figure 18: Optimal mode S. (a) Time evolution of the kinetic energy budget. (b) Time evolution of the barycenter position. $dX_m/dt \approx 0.79$ (in dashed-line).

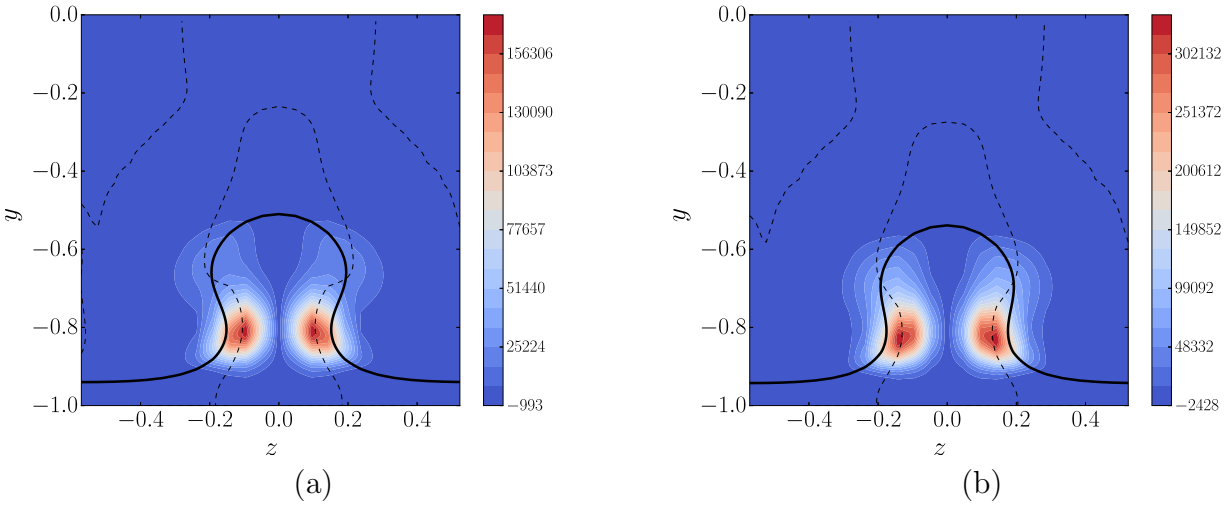

Figure 19: Optimal mode S. Production term T_z at $t = 3$ (a) and $t = 5$ (b) for $x_i = X_m\,(t = 3) = 8.3$ and $x_i = X_m\,(t = 5) = 9.8$, respectively. Full line represents the position where $U = dX_m/dt$. Dashed-lines represents positions of spanwise inflection points.

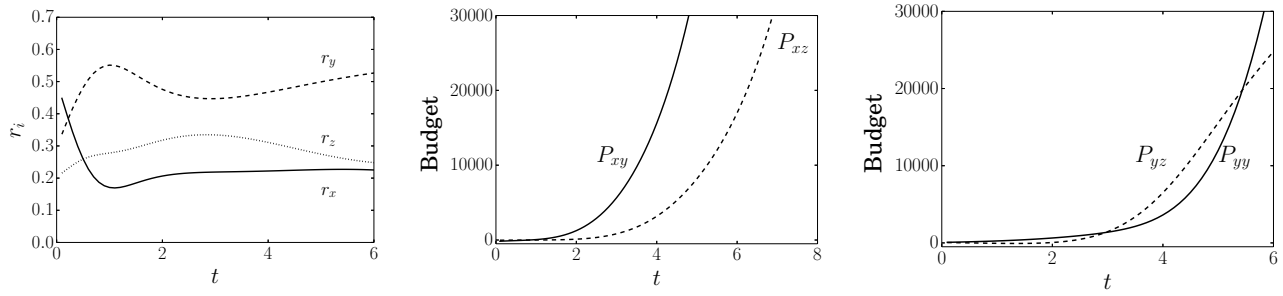

(a) (b) (c)

Figure 20: Optimal mode S. (a) Time evolution of r_x, r_y and r_z. Vorticity budget for Ω'_x (b) and Ω'_y (c).

the spanwise direction as classically found for the exponentially growing sinuous mode [11]. It also supports that for large times the S is governed by an exponential growth similarly as the one predicted by a local stability theory.

Figure 20 (a) displays the ratio of enstrophy components as a function of time. It is interesting to notice that vorticity transfers exhibit the same behaviour than V_{22} when we replace r_y into r_z. In particular, at $t = 0$, the vorticity is mainly composed of Ω'_x and Ω'_y. For $t < 3$, we observe a transfer from the streamwise vorticity to the wall-normal vorticity characteristic of a lift-up mechanism associated with the wall-normal shear. This mechanism is associated with the tilting term due to the wall-normal basic shear as shown in figure 20 (c). In addition, the figure 20(a) also shows an almost constant value of the spanwise vorticity contribution for short times. The latter mechanism can be attributed to a Orr-mechanism that results for the wall-normal shear. Finally, for $t \geq 3$, where the mode is dominated by a mechanism associated with a point of inflection, the time evolution of enstrophy ratio reaches an equilibrium stage that is accompanied by a production of streamwise vorticity mainly governed by the wall-normal shear as t is increased.

4 Optimal modes: nonlinear evolution

We will now analyze the nonlinear effects induced by the mechanisms described above. For that purpose, the optimal modes are superimposed to the streaky base flow with a given initial amplitude and the full Navier-Stokes equations are integrated forward in time (see table 1 for flow cases). Being interested in describing the different stages leading to a turbulent flow, we consider hereafter four spanwise wavelength ($\approx 4.6\ h$). When considering a fully developed turbulent channel flow, large-scale motions have a characteristic spanwise size of the order of $2\ h$ [41]. The latter remark may give us some confidence that the spanwise extension considered in our case is sufficient. The time evolution of the kinetic energy associated with flow disturbances are extracted from DNS by subtracting the instantaneous state of the velocity field from the secondary base flow. In figure 21 (a) and (b), we report time evolutions of kinetic energy disturbances associated with V_{11} and V_{12} (i.e. $t_{opt} = 2$) for $A_0 = 0.015$ and $A_0 = 0.025$, respectively. One may recall that for $A_0 = 0.015$ the secondary base flow is asymptotically stable with respect to varicose perturbations in a local framework and for $A_0 = 0.025$ two types

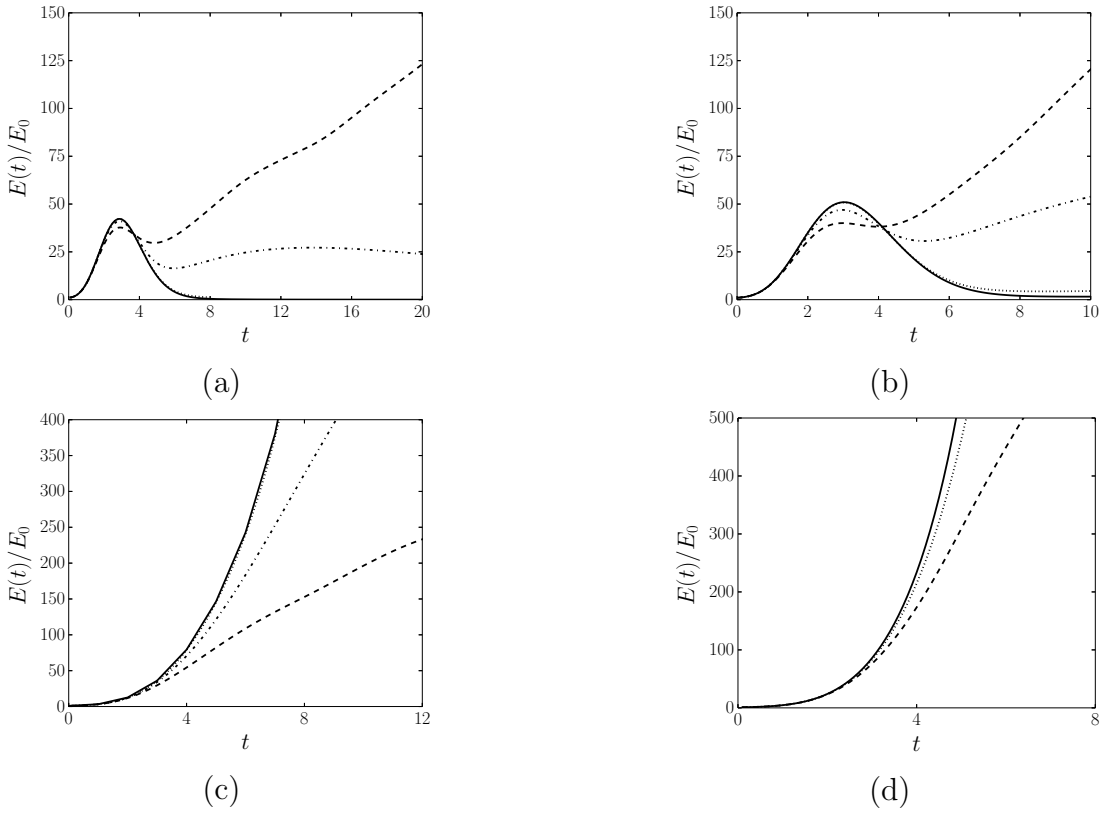

Figure 21: Nonlinear simulations. Integrated kinetic energy for the perturbation versus time. (a) V_{11}; (b) V_{12}; (c) V_{22} and (d) S. $E_0 = 10^{-8}$ (...), $E_0 = 2.5 \times 10^{-7}$ (▬ ▬ ▬) and $E_0 = 10^{-6}$ (▬ ▬ ▬). The linear evolution is represented in (▬▬▬).

of optimal wavepackets (i.e. V_{12} and V_{22}) coexist. We first focus on the flow case $A_0 = 0.015$ depicted in figure 21 (a). For E_0 below 2.5×10^{-7}, the kinetic energy for disturbances is damped for long times. When the initial amplitude of the mode is increased above the former value, we observe a strong increase in kinetic energy around $t = 5$ where the curve departs from linear regime. The figure 21 (b) shows result for the flow case $A_0 = 0.025$. For the smallest amplitude $E_0 = 10^{-8}$, the kinetic energy evolution exhibits a similar behaviour to the one obtained in a linear framework. When the initial amplitude of the optimal mode is fixed to $E_0 = 2.5 \times 10^{-7}$, the kinetic energy undergoes a different path. For $t > 5$, while disturbances are temporally damped in the linear regime, a growth of the kinetic energy is observed due to nonlinearity. As can be expected, the critical initial energy for disturbances to trigger a subcritical secondary instability is increased when the streak amplitude decreases. Furthermore, for V_{11} and V_{12}, nonlinear trajectories are seen to be separated by an edge state for given values of A_0 and E_0 (see Duguet et al. [42] for instance).

Hereafter, we restrict our analysis to $A_0 = 0.025$. We plot in figures 21 (c) and (d), the time evolution of kinetic energy associated with disturbances for modes V_{22} and S. For both modes, nonlinearities have a stabilizing effect characteristic of a supercritical behaviour.

Figure 22 (a), (b) shows vortical structures at $t = 3.5$ and $t = 5.75$ associated with the nonlinear development of V_{12} for $t_{opt} = 2$ and $E_0 = 10^{-6}$. For short times, the effect of Orr/lift-up mechanism on the low-speed streak produces slightly inclined streamwise vortex pair (see

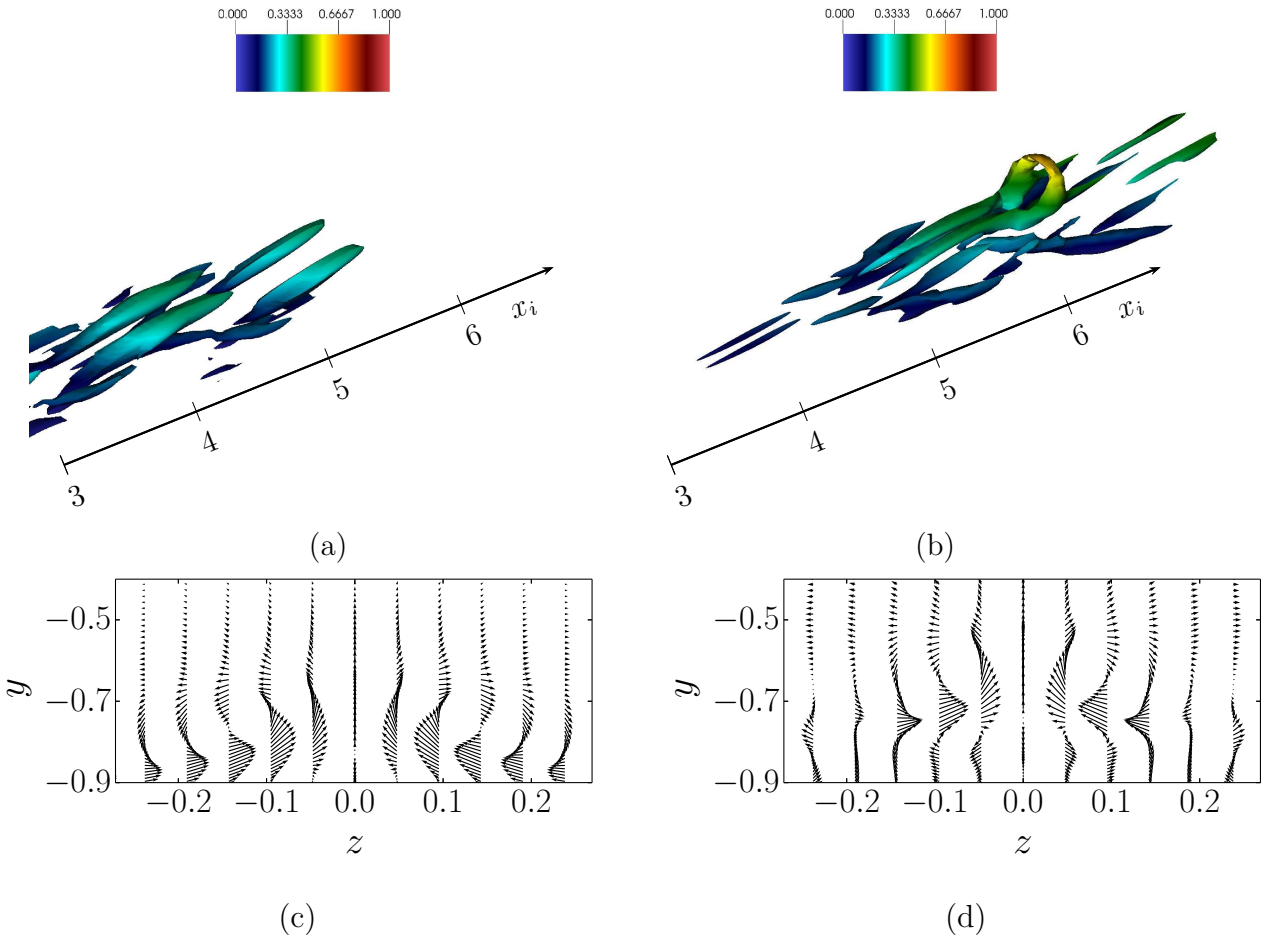

Figure 22: Varicose case V_{12}. Nonlinear simulation for $E_0 = 10^{-6}$. Visualization is restricted to one low-speed streak. The coherent structures are identified with isosurfaces of λ_2 criterion in (a) and (b) for $t = 3.5$ and $t = 5.75$, respectively, coloured by the distance from the lower wall. The vector field (w, v) in the cross section (z, y) is shown for $t = 3.5$ and $t = 5.75$ at $x_i = 4$ and $x_i = 5.8$ in panels (c) and (d), respectively where $w = \overline{W} - W$ and $v = \overline{V} - V$.

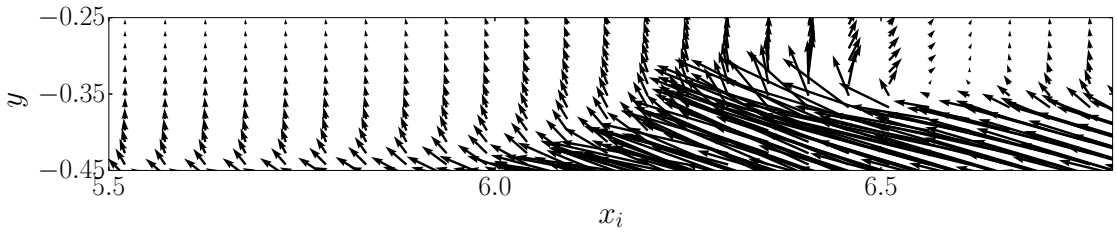

Figure 23: Varicose case V_{12}. Nonlinear simulation for $E_0 = 10^{-6}$. Vector plots of perturbation velocity ($u = \overline{U} - U$ and $v = \overline{V} - V$) on (x, y) plane at extracted at the center of a low-speed streak.

figure 22(a)). As time evolves, between the two legs of the vortex pair, fluid is pumped up and backwards. It induces the formation of an hairpin head that is lifted-up from the wall and shaped into a ring vortex as shown in figures 22 and 23. This event ($u < 0$, $v > 0$; Q_2 event in the quadrant analysis) is accompanied by an abrupt increase in the kinetic energy associated with disturbances as reported in figure 21 (b). Further downstream (see figure 24), we observe that the vortex legs collide due to self-induction and generate a secondary hairpin vortex. This mechanism has already been observed in a fully turbulent regime by Zhou et al. [43]. This whole process takes place in a region where linear analysis of secondary base flow concludes of asymptotic stability in a local framework. This hairpin regeneration is still accompanied with an increase in kinetic energy for disturbances.

Regarding V_{22}, a different behaviour is observed. For short times the varicose mode V_{22} grows rapidly under the action of a quasi-exponential instability. When nonlinearities play a significant role, the mode exhibits a train of arch-like structures as shown in figure 25 (a). By contrast with V_{12}, vortical structures for V_{22} are not attached to the wall and arches are not self-generated from one flow pattern but rather result from nonlinear saturation effects of the instability mode. The figure 25 also shows that characteristic structures of V_{22} are quasi-streamwise vortices joining in the middle of the low-speed streak and also vortices pointing downstream taking a V shape. These vortices are very similar with those observed in the simulations of varicose streak breakdown for a flat plate boundary layer by Brandt [12]. Due to nonlinearities both V_{22} and V_{12} exhibit a bridge-like structure connecting quasi-streamwise vortices identified on both sides of the low-speed streak in the linear regime.

The initial stage of the nonlinear evolution of S is shown in figure 25(b). The underlying vortical structures take the form of quasi-streamwise streamwise vortices located on both sides of the low-speed streak. In particular, vortices alternating in the streamwise direction are localized the center of the low-speed streak. The latter nonlinear sinuous scenario exhibits close similarities with the sinuous streak breakdown described by Brandt and Schlatter [44] for the case of a flat plate boundary layer.

5 Paths to turbulence

While in the previous section we observe initial stages of the nonlinear regime, it is not straightforward that it should effectively provoke transition. Therefore, the investigation of the nonlinear evolution for final stages of transition for such optimal wavepackets is worthwhile. Hereafter,

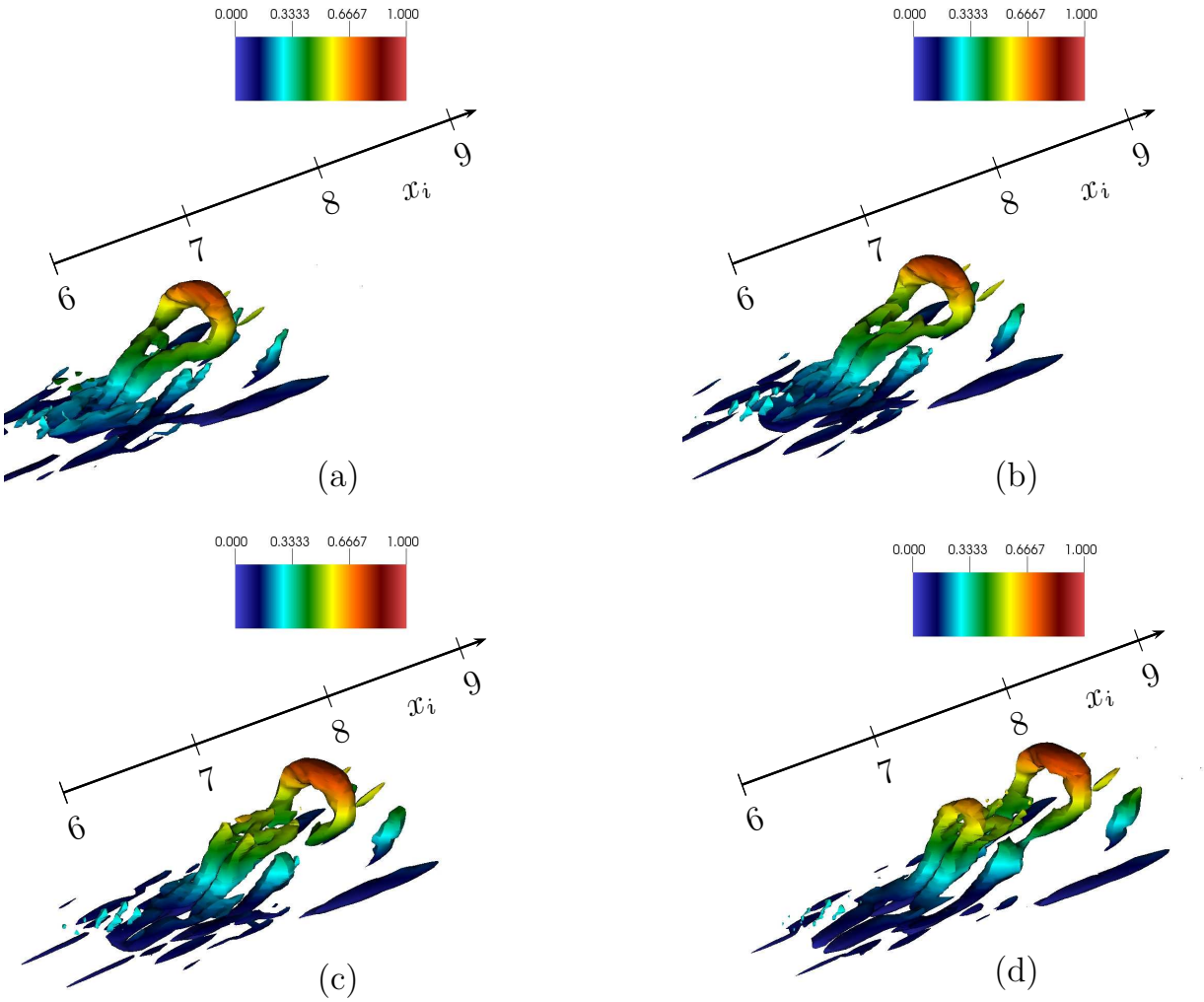

Figure 24: Varicose case V_{12}. Nonlinear simulation for $E_0 = 10^{-6}$. Visualization is restricted to one low-speed streak. The coherent structures are identified with isosurfaces of λ_2 criterion in (a), (b), (c) and (d) for $t = 7.5$, 8, 8.5 and 9, respectively, coloured by the distance from the lower wall.

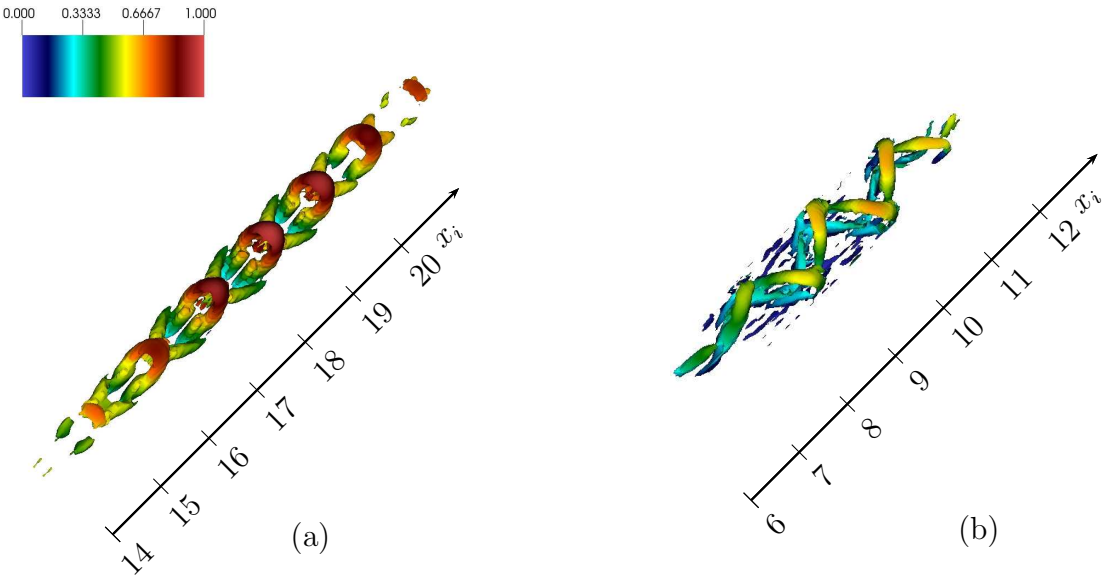

Figure 25: Nonlinear simulation for $E_0 = 10^{-6}$. Visualization is restricted to one low-speed streak. The coherent structures are identified with isosurfaces of λ_2 criterion for $t = 5$ coloured by the distance from the lower wall. (a) Varicose mode V_{22}; (b) Sinuous mode S.

only the case $A_0 = 0.025$ is considered.

Let us first examine the evolution of instantaneous flow structures as the wavepacket evolves along the streamwise direction. We show in figure 26 instantaneous snapshots of vortical structures developing inside the boundary layers for V_{12}, V_{22} and S at times $t = 20$, 40 and 60 where the λ_2 criterion coloured by the distance from the lower wall is considered. For V_{12}, figure shows that for $t = 20$, the subcritical mechanism described in the previous section has led to the formation of a hairpin train similar as the mechanism described by Zhou et al. [43]. For time $t = 40$, the wavepacket spreads streamwise, and we observe a turbulent puff in the center of the latter surrounded by more quiet phases upstream and downstream. Furthermore, while the leading edge of the wavepacket is dominated by ring-like structure (or Ω vortices) extending near the wall, the downstream part is characterized by arch-like structures (i.e. not attached to the wall) developing in the outer part of the boundary layer. For time $t = 60$, we observe that the puff has spreat in the streamwise direction and that arch-like structures predominate. This laminar/turbulent transition process is similar to the one described by G. Eitel-Amor and Schlatter [45] where the authors investigate the flat plate boundary layer case.

When considering transition induced by V_{22}, figure 26 shows that for $t = 20$ the flow is populated by trains of arch-like structures. Their tips are deformed into vortex ring types and tilted upward from the wall in the outer part of the boundary layer. In the center of the wavepacket, ring like structures split generating harmonics which is not observed for V_{12} at the same time. At $t = 40$, arch-like structures predominate in the flow and we observe the breakdown of the spanwise symmetry. For $t = 60$, the wavepacket extends on a larger distance than the one associated with V_{12}.

For the nonlinear evolution of the sinuous mode S, figure 26 shows that for $t = 20$ higher harmonics are generated than for the case V_{22} at the same time. In addition, flow already breaks symmetry in the spanwise direction at this time. We also observe that while the leading edge of the wavepacket is characterized by a sinuous motion, the center of the latter is dominated

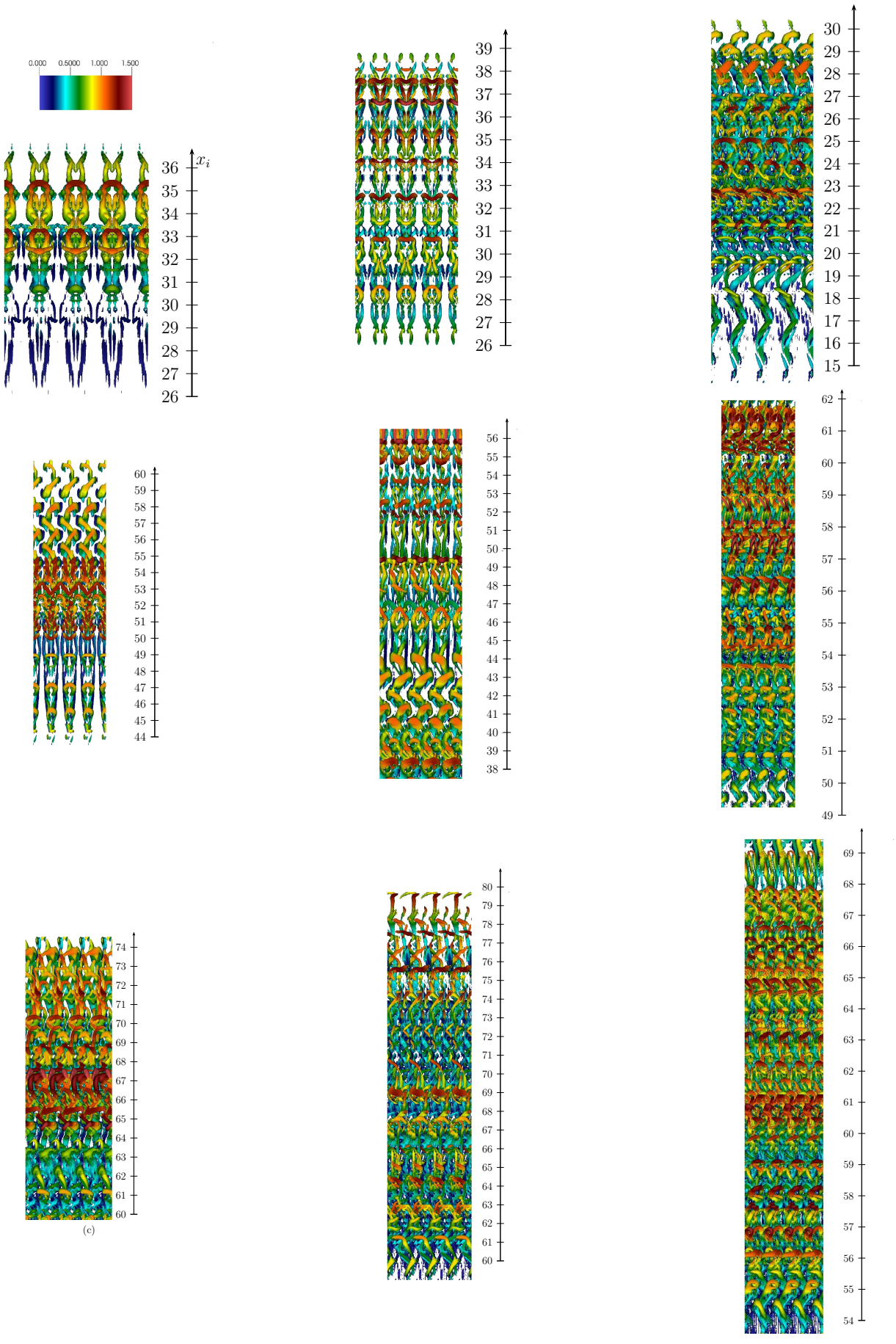

Figure 26: $E_0 = 10^{-6}$. Isosurfaces of the λ_2 criterion are shown coloured by the distance from the lower wall at $t = 20$, 40 and 60 respectively for V_{12}, V_{22} and S (from the left to the right).

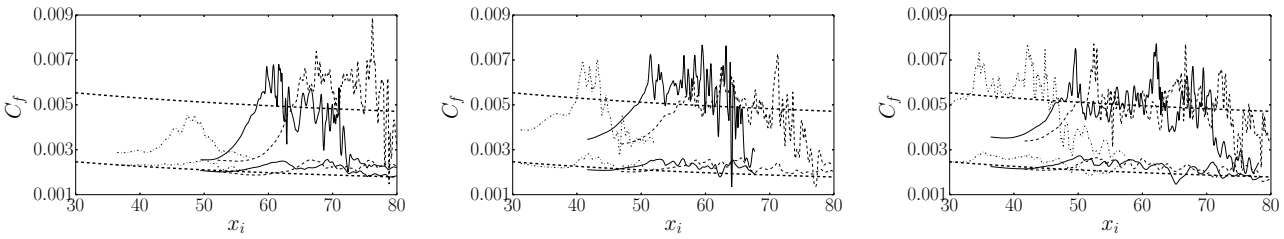

(a) (b) (c)

Figure 27: $E_0 = 10^{-6}$. Skin friction coefficient versus the streamwise position for $t = 48$, 64 and 72 (in dotted, full and dashed lines, respectively). The lowest and highest dashed lines represent the distribution of C_f for the laminar and turbulent cases, respectively. (a) V_{12}, (b) V_{22} and (c) S.

by similar coherent motions as the one observed for V_{12} and V_{22} such as arch-like structures. Hence, figure 26 gives some arguments that for both scenario, V_{12}, V_{22} and S evolve into a unique turbulent state as also observed by G. Eitel-Amor and Schlatter [45] and T. Sayadi and Moin [46] in the case of a turbulent flat plate boundary layer.

In figure 27, we show the skin friction C_f as a function of x_i for the different modes. For comparison purposes, we also report C_f values found in literature for a turbulent boundary layer and the laminar case. The spanwise average instantaneous streamwise velocity is considered to evaluate the skin friction coefficient. Considering that C_f provides an indication of the transition location, the figure 27 shows that for $t = 48$, transition occurs for both S and V_{22}. For V_{12}, transition is established for $t > 50$. The latter remark is consistent with the discussion above related to the observation of coherent structures. It is also interesting to note that the subcritical transition provided by V_{12} yields similar C_f than for S and V_{22} cases. For both cases, while for the lower wall, transition is observed for $t = 64$ and later, the transition is not yet triggered for the boundary layer developing along the upper wall.

Statistics are now investigated. We consider a temporal window where C_f reaches a value close to its turbulent case. For all cases, the streamwise position where statistics are collected is set to $x_i = 66$. Assuming a spanwise periodicity, a spanwise average is also performed. 100 velocity fields are collected every 10 time steps which gives a data sample size of 9600. The friction Reynolds number (i.e. based on the friction velocity, the half-channel heigth and the kinematic viscosity) at the lower wall is found for all flow cases equal to $Re_\tau = 166$. Hereafter, the superscript + will denote quantities scaled in inner units. Figure 28 shows the mean streamwise velocity profile in the wall normal direction. For the lower wall, it exhibits a flatter profile in comparison with its upper wall counterpart. It gives some evidence that the flow evolves to a turbulent regime on the lower wall. To further investigate the latter remark, we report in figure 29, the streamwise average velocity together with the rms velocities as a function of the distance from the lower wall in inner units. For comparison purposes, results provided by Moser et al. [47] and Schlatter and Orlu [48] for a turbulent channel flow at $Re_\tau = 180$ and a turbulent flat plate boundary layer at $Re_\tau = 252$ are also shown. Despite the lack of convergence of statistics due to the small data samples that are collected, a good agreement for the mean velocity profile is observed in figures 29 (a),(c) and (e). Regarding the variance of the mean velocity components, the figures 29 (b),(d) and (f) show that profiles are also in good agreement with literature. In particular, the streamwise velocity dominates in the r.m.s values

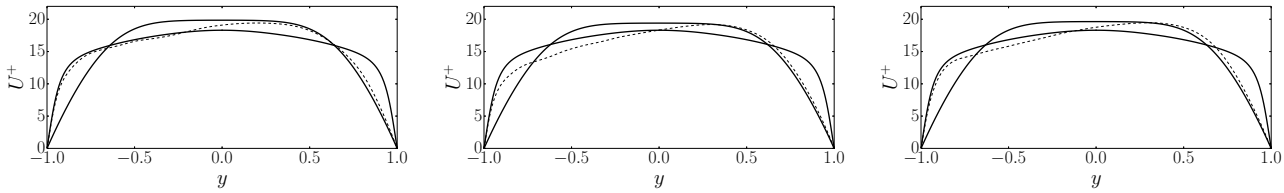

Figure 28: $E_0 = 10^{-6}$ and $x_i = 66$. Mean streamwise velocity dimensionless by u_τ estimated at $y = -1$. In full line, the distributions of U^+ for a fully developed turbulent channel flow at $Re_\tau = 180$ and for the laminar entrance channel flow are reported. (a) V_{12}, (b) V_{22} and (c) S.

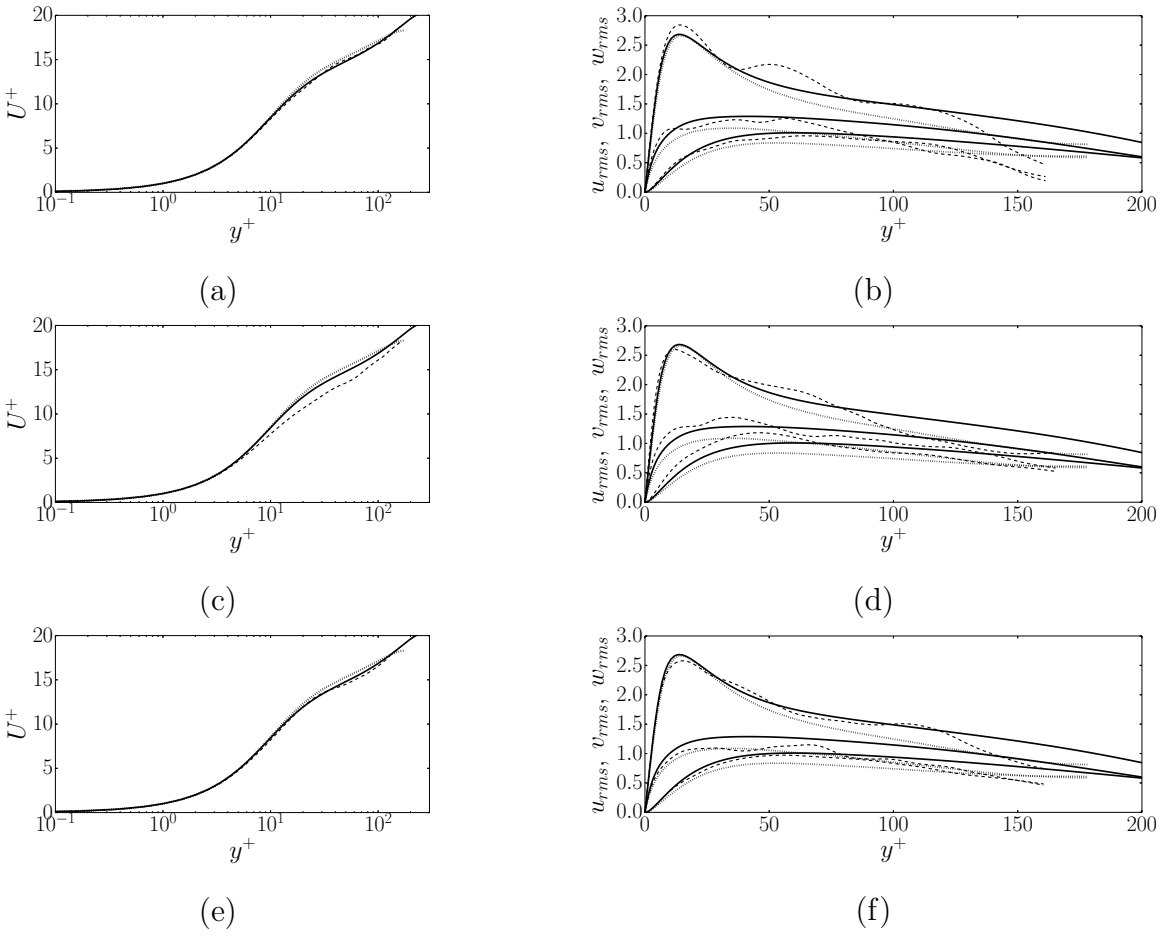

Figure 29: $E_0 = 10^{-6}$ and $x_i = 66$. In dashed lines: (a),(c) and (e) mean streamwise velocity profiles versus the distance from the wall in inner units; (b),(d) and (f) rms profiles versus the distance from the wall in inner units. Profiles for a fully developed turbulent channel flow at $Re_\tau = 180$ and a turbulent flat plate boundary layer at $Re_\tau = 252$ are also reported in full and dotted lines, respectively. (a,b) V_{12}, (c,d) V_{22} and (e,f) S.

and it peaks at a distance from the lower wall in inner units $y^+ \approx 13$. It thus provides insight that streaks associated with a self-sutained process in the buffer region are present which is an universal characteristic of wall-turbulence [49]. Hence, it shows that statitistics converge to the same turbulent values in each cases that are considered. Finally, for all flow cases, we note that turbulent coherent structures populating the outer part of the boundary layer have not triggered yet turbulent transition of the boundary layer developping on the upper wall. It gives some insight on the fact that the turbulent transition of boundary layers developing along upper and lower wall in the entrance channel flow can remain uncoupled on a long distance.

6 Conclusions

This work aims at describing different paths leading to turbulence for the entrance channel flow case under subcritial conditions. The present study focuses on the case where upstream conditions are associated with an uniform flow. The flow cases that are investigated are such that perturbations are injected quite near the channel entrance and the subsequent turbulent transition occurs in the developing boundary layers. In this context, a specific attention has been paid to understand both linear and nonlinear mechanisms bringing the system to transition. Due to the favorable pressure gradient, the turbulent/transition path excludes an exponentially growing Tollmien-Schlichting mode, and is based on secondary instability of streaks. To generate the streaks, a pair of optimal streamwise vortices (i.e. having the highest potential for transient energy growth in a local framework) is superimposed to the boundary layer developing along one of the two walls, at the inflow plane. Three different streaks amplitudes are considered. Under a locally flow assumption, all of them are seen to be unstable with respect to a sinuous temporal linear instability. While the lowest streak amplitude case is stable for varicose modes at all streamwise positions, the high amplitude flow cases exhibit a varicose instability.

A linear global optimization has been performed consisting in searching for initial perturbations having the largest energy growth for given times. Specifically, we consider varicose and sinuous symmetry separately and only the fundamental case (i.e. streaks and perturbations have same spanwise periodicity). Optimal perturbations at the initial time take the form of localized wavepackets for all cases. Sinuous wavepackets are dominant for the lowest streak amplitude whereas the varicose secondary perturbation is the most amplified for the largest streak amplitude. However, for short optimization times, varicose and sinuous optimal wavepackets attain comparable gain in energy. Interestingly, while the sinuous optimal wavepacket is not too affected by time optimization, varicose ones exhibit two different behaviors. For short optimization times, varicose perturbation at initial time is localized in the flanks of the low-speed streak near the inlet and for larger target times, the initial wavepacket is concentrated downstream where streaks are subjected to exponential instability. For the sinuous wavepacket, the mechanism responsible for energy growth is mainly associated with the spanwise shear and especially the presence of inflection points along spanwise direction, as usually found for the streaks instability. For the varicose symmetry, the optimal perturbation corresponding to short target times extracts energy from the base flow by combining Orr and lift-up mechanisms. By inspecting the vorticity budget, it is shown that the lift-up mechanism is governed by a vortex tilting term associated with the spanwise shear. This mechanism exhibits similarities with the one described by Cherubini et al. [23] for a streaky flow behind a bump in a flat plate bound-

ary layer. For larger optimization times, the energy growth is associated with the presence of inflection point in the wall normal direction as revealed by the kinetic energy production terms distribution in the cross-sections.

By means of direct numerical simulations, the nonlinear space-time dynamics of optimal wavepackets is investigated. We observe the existence of a path to turbulence which is subcritical with respect to secondary modal instability for the varicose wavepacket associated with short optimization time. This nonlinear path leads to hairpin trains that breakdown to turbulence downstream. For larger optimization times, where perturbations are dominated by modal instability, nonlinearities first have a damping effect on the energy growth of perturbation, typical of a supercritical behaviour. As the perturbation moves downstream, the varicose optimal wavepacket leads to arch-likes structures in the outer part of the boundary layer, and spanwise oscillating streaks are observed for the sinuous one. Further downstream, we observe the convergence to characteristic wall-bounded turbulent flow profiles (mean flow and r.m.s) for all cases. In this stage, the outer part of the boundary layer is dominated by arch-like patterns independently of the symmetry of the initial wavepacket.

These result lead us to bring some conclusions: (a) the entrance channel flow may exhibit laminar/turbulent transition well before the merging of the developing boundary layers (b) the fully developed turbulent region exhibits similar statistics as those associated with wall-bounded turbulent flows; as a consequence it seems difficult to distinguish either or not laminar/turbulent transition observed in channel flow experiments is due to entrance effects (c) varicose wavepackets associated with short optimization times are localized near the inlet and have comparable gains with their sinuous counterparts. It further indicates that under certain conditions of external perturbations, the varicose scenario leading to streak breakdown and turbulence can be viable even if streaks are stable with respect to modal instability under the parallel flow assumption; (d) for the values of Re and x_0 (i.e. streamwise abscissa of the intial vortex pair generating streaks) that are considered, the upper and lower boundary layers are weakly mutually dependent. The present study brings some light on the transient varicose instability observed by Buffat et al. [5] using DNS. In this respect, the use of global optimization gives an accurate description of the transient/convective instability mechanism in a region where nonparallelism effects can not be neglected. Nevertheless questions remain unanswered. Among some of them, it is questionable how the subcritical scenario observed for the varicose mode is affected by the streak amplitude. In particular, does the subcritical varicose scenario lead to a turbulent flow for streak amplitudes that are lower than critical values giving rise to sinuous exponential mode ? Furthermore, the present work only focuses onto a specific choice of inflow condition. Sadri and Floryan [4] shows that for upstream conditions associated with a sharp-edge channel, the flow exhibits separation zones on both walls that extend far downstream when increasing the Reynolds number. Hence, it may be suggested a different scenario leading to turbulence for such entrance channel flow solution, strongly connected to separated flow unsteadiness similar as those reported by Passaggia et al. [50].

References

[1] A.A. Draad, G.D.C. Kuiken, and F.T.M. Nieuwstadt. Laminar-turbulent transition in pipe flow for Newtonian and non-Newtonian fluids. *J. Fluid Mech.*, 377:267–312, 1998.

[2] D. Biau. Linear stability of channel entrance flow. *Euro. J. of Mech.-B/Fluids*, 27:579–590, 2008.

[3] M. Asai and J.M. Floryan. Certain aspects of channel entrance flow. *Physics of Fluids*, 16:1160–1163, 2004.

[4] R.M. Sadri and J.M. Floryan. Entry in a channel. *Computers & Fluids*, 31:133–157, 2002.

[5] M. Buffat, L. Le Penven, A. Cadiou, and J. Montagnier. DNS of bypass transition in entrance channel flow induced by boundary layer interaction. *Euro. J. of Mech.-B/Fluids*, 43:1–13, 2014.

[6] M.T. Landhal. A note on an algebraic instability of invscid parallel shear flow. *J. Fluid Mech.*, 98:243–251, 1980.

[7] M. Buffat, L. Le Penven, and A. Cadiou. An efficient spectral method based on an orthogonal decomposition of the velocity for transition analysis in wall bounded flow. *Computers & Fluids*, 42:62–72, 2011.

[8] L. Brandt and D.S. Henningson. Transition of streamwise streaks in zero-pressure-gradient boundary layers. *J. Fluid Mech.*, 472:229–261, 2002.

[9] T.A. Zaki and P.A. Durbin. Mode interaction and the bypass route to transition. *J. Fluid Mech.*, 531:85–111, 2005.

[10] P. Durbin and X. Wu. Transition beneath vortical disturbances. *Annu. Rev. Fluid Mech.*, 39:107–128, 2007.

[11] P. Andersson, L. Brandt, A. Bottaro, and D.S. Henningson. On the breakdown of boundary layer streaks. *J. Fluid Mech.*, 428:29–60, 2001.

[12] L. Brandt. Numerical studies of the instability and breakdown of a boundary-layer low-speed streak. *Euro. J. of Mech.-B/Fluids*, 26:64–82, 2007.

[13] M. Matsubara and P.H. Alfredsson. Disturbance growth in boundary layers subjected to free-stream turbulence. *J. Fluid Mech.*, 430:149–168, 2001.

[14] A.C Mandal, L. Venkatakrishnan, and J. Dey. A study of boundary layer transition induced by freestream turbulence. *J. Fluid Mech.*, 660:114–146, 2010.

[15] N.J. Vaughan and T. A. Zaki. Stability of zero-pressure-gradient boundary layer distorted by unsteady Klebanoff streaks. *J. Fluid Mech.*, 681:116–153, 2011.

[16] M.J.P. Hack and T.A. Zaki. Streak instabilities in boundary layers beneath free-stream turbulence. *J. Fluid Mech.*, 741:280–315, 2014.

[17] L. Brandt and H.C. de Lange. Streak interactions and breakdown in boundary layer flows. *Physics of Fluids*, 20:024107, 2008.

[18] W. Schoppa and F. Hussain. Coherent structure generation in near-wall turbulence. *J. Fluid Mech.*, 453:57–108, 2002.

[19] J. Hoepffner, L. Brandt, and D.S. Henningson. Transient growth on boundary layer streaks. *J. Fluid Mech.*, 537:91–100, 2005.

[20] C. Cossu, M. Chevalier, and D.S. Henningson. Optimal secondary energy growth in a plane channel flow. *Physics of Fluids*, 19:058107, 2007.

[21] W. M. F. Orr. The stability or instability of the steady motions of a perfect liquid and of a viscous liquid. part i: A perfect liquid. part ii: A viscous liquid. *Proc. R. Irish Acad. A*, 27:9–37, 1907.

[22] C. Cossu, L. Brandt, S. Bagheri, and D.S. Henningson. Secondary threshold amplitudes for sinuous streak breakdown. *Physics of Fluids*, 23:074103, 2011.

[23] S. Cherubini, M.D. De Tullio, P. De Palma, and G. Pascazio. Transient growth in the flow past a three-dimensional smooth roughness element. *J. Fluid Mech.*, 724:642–670, 2013.

[24] R.D. Moser, P. Moin, and A. Leonard. A spectral numerical method for the Navier-Stokes equations with applications to Taylor-Couette flow. *J. Comput. Phys.*, 52:524–544, 1983.

[25] F.P. Bertolotti, T. Herbert, and P.R. Spalart. Linear and nonlinear stability of the Blasius boundary layer. *J. Fluid Mech.*, 242:441–474, 1992.

[26] J. Nordstrom, N. Nordin, and D. Henningson. The fringe region technique and the Fourier method used in the direct numerical simulation of spatially evolving viscous flows. *SIAM J. Sci. Comput.*, 20:1365–1393, 1999.

[27] F. Alizard, J.-C. Robinet, and X. Gloerfelt. A domain decomposition matrix-free method for global linear stability. *Computers & Fluids*, 66:63–84, 2012.

[28] P.R. Spalart, R. D. Moser, and M.M. Rogers. Spectral methods for the Navier-Stokes equations with on infinite and two periodic conditions. *J. Comput. Phys.*, 96:297–324, 1990.

[29] L. Brandt, C. Cossu, J.-M. Chomaz, P. Huerre, and D.S. Henningson. On the convectively unstable nature of optimal streaks in boundary layers. *J. Fluid Mech.*, 485:221–242, 2003.

[30] D. Barkley, H.M. Blackburn, and S.J. Sherwin. Direct optimal growth analysis for timesteppers. *Int J. for Num. Methods in Fluids*, 57:1435–1458, 2008.

[31] A.K. Kapila, G.S.S. Ludford, and V.O.S. Olunloyo. Entry flow in a channel. part 3. inlet in a uniform stream. *J. Fluid Mech.*, 57:769–784, 1972.

[32] F. Durst, S. Ray, B. Ünsal, and O. A. Bayoumi. The development lengths of laminar pipe and channel flows. *Journal of Fluids Engineering*, 127:1154–1160, 2005.

[33] P.J. Schmid and D.S. Henningson. *Stability and Transition in Shear Flows.* Applied Mathematical Sciences 142, Springer, 2001.

[34] F. Alizard, J.-C. Robinet, and G. Filliard. Sensitivity analysis of optimal transient growth for turbulent boundary layers. *Euro. J. of Mech.-B/Fluids*, 49:373–386, 2015.

[35] F. Alizard. Linear stability of optimal streaks in the log-layer of turbulent channel flows. *Physics of Fluids*, 27:105103, 2015.

[36] M. O. John, D. Obrist, and L. Kleiser. Secondary instability and subcritical transition of the leading-edge boundary layer. *J. Fluid Mech.*, 792:682–711, 2016.

[37] A. Monokrousos, E. Akervik, L. Brandt, and D.S. Henningson. Global three-dimensional optimal disturbances in the Blasius boundary-layer flow using time-steppers. *J. Fluid Mech.*, 650:181–214, 2010.

[38] C. Cossu and L. Brandt. On Tollmien-Schlichting-like waves in streaky boundary layers. *Euro. J. of Mech.-B/Fluids*, 23:815–833, 2004.

[39] O.T. Schmidt, S. M. Hosseini, U. Rist, A. Hanifi, and D.S. Henningson. Optimal wavepackets in streamwise corner flow. *J. Fluid Mech.*, 766:405–435, 2015.

[40] K.M. Butler and B.F. Farrell. Three-dimensional optimal perturbations in viscous shear flow. *Physics of Fluids*, A4:1637, 1992.

[41] J.C. Del Alamo and J. Jimenez. Spectra of the very large anisotropic scales in turbulent channels. 5:41–44, 2003.

[42] Y. Duguet, P. Schlatter, D.S. Henningson, and B. Eckhardt. Self-sustained localized structures in a boundary-layer flow. *Physical Review Letters*, 108:044501, 2012.

[43] J. Zhou, R.J. Adrian, S. Balachandar, and T.M. Kendall. Mechanisms for generating coherent packets of hairpin vortices in channel flow. *J. Fluid Mech.*, 387:353–396, 1999.

[44] L. Brandt and P. Schlatter. Transition in boundary layers subject to free-stream turbulence. *J. Fluid Mech.*, 517:167–198, 2004.

[45] O. Flores G. Eitel-Amor and P. Schlatter. Hairpin vortices in turbulent boundary layers. *Journal of Physics: conference series*, 506:012008, 2014.

[46] C. W. Hamman T. Sayadi and P. Moin. Direct numerical simulation of complete H-type and K-type transitions with implications for the dynamics of turbulent boundary layers. *J. Fluid Mech.*, 724:480–509, 2013.

[47] R.D. Moser, J. Kim, and N.N. Mansour. Direct numerical simulation of turbulent channel flow up to $Re_\tau = 590$. 11:943–945, 1998.

[48] P. Schlatter and R. Orlu. Assessment of direct numerical simulation data of turbulent boundary layers. *J. Fluid Mech.*, 659:116–126, 2010.

[49] J. M. Hamilton, J. Kim, and F. Waleffe. Regeneration mechanisms of near-wall turbulence structures. *J. Fluid Mech.*, 287:317–348, 1995.

[50] P.Y. Passaggia, T. Leweke, and U. Ehrenstein. Transverse instability and low-frequency flapping in incompressible separated boundary layer flows: an experimental study. *J. Fluid Mech.*, 703:363–373, 2012.